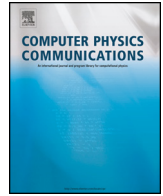




ELSEVIER

Contents lists available at ScienceDirect

Computer Physics Communications

journal homepage: www.elsevier.com/locate/cpc

Computational Physics

Vlasov-Fokker-Planck-Maxwell simulations for plasmas in inertial confinement fusion [☆]S.T. Zhang ^a, X.M. Li ^a, D.J. Liu ^a, X.X. Li ^a, R.J. Cheng ^a, S.Y. Lv ^a, Z.M. Huang ^a, B. Qiao ^b, Z.J. Liu ^{a,b,*}, L.H. Cao ^{a,b}, C.Y. Zheng ^{a,b}, X.T. He ^{a,b}^a Institute of Applied Physics and Computational Mathematics, Beijing, 100088, People's Republic of China^b Center for Applied Physics and Technology, HEDPS, and State Key Laboratory of Nuclear Physics and Technology, School of Physics, Peking University, Beijing, 100871, People's Republic of China

ARTICLE INFO

Article history:

Received 25 February 2023

Received in revised form 10 August 2023

Accepted 6 September 2023

Available online 12 September 2023

Keywords:

Inertial confinement fusion

Plasma simulation

Plasma transport processes

Fokker-Planck

TVD scheme

Laser-plasma interactions

ABSTRACT

This work presents a code to simulate collisions and laser-plasma interactions of multiple-species plasmas by solving 1D3V Vlasov-Fokker-Planck-Maxwell equations. The distribution functions of all species are expanded into spherical harmonic series of arbitrary order. Each electron or ion species possesses its distinct and suitable velocity mesh and the number of harmonics. Collisions between different ion species are considered and treated with the Fokker-Planck collision term. The code employs the total variation diminishing (TVD) scheme to avoid numerical instabilities in the region of steep density, rarefied plasma-vacuum interface, and non-periodic boundary conditions, which makes it possible to simulate cases that are close to actual physical scenes. The number of particles is globally conserved for each species, the energy for each species is conserved for collisions between the same species, and total energy is conserved for collisions between different species.

© 2023 Elsevier B.V. All rights reserved.

1. Introduction

Collisions among particles play an important role in laser-plasma interactions in recent research, which involves many processes such as thermal equilibrium, thermal transport [1–5], plasma heating [6–8], laser-plasma instabilities, and so on. In indirect-drive inertial confinement fusion, the ionized collisional plasma fills the hohlraum and interacts with the laser [9–13], causing various instabilities such as Brillouin instability and Raman instability [14–21]. Collisions can also affect the damping rate by generating collisional damping, affecting Landau damping, and heating electrons and ions, thereby affecting the intensity of the scattered light [22–24]. In fast ignition inertial confinement fusion, relativistic electrons are transported from the critical surface to the boundary of the compressed fusion fuel, where the energy deposition is contributed by plasma heat conduction [25–34]. Besides, the kinetic effect is often obvious for electrons and low-Z ions [35,36]. To study these cases, the velocity distribution of electrons and ions should be considered, and the system should be treated with kinetic theory. When studying laser-plasma interactions (LPI), even in the 1D configuration space, the 3D description of the distribution function in the velocity space is still necessary to describe the anisotropy caused by the external laser field or magnetostatic field.

The Fokker-Planck equation describes the kinetic evolution of the collisional plasma systems. It is necessary to develop a code to simulate the laser-plasma systems by solving the Fokker-Planck equation combined with Maxwell equations. Compared to hydrodynamic simulation, it takes into account the microscopic information of the distribution function and can simulate the non-equilibrium system with the distribution function deviating from Maxwellian distribution. Particle-in-cell (PIC) simulation is another tool to study various nonlinear effects in the interaction between laser and plasma, which has been widely developed in recent years, but it has inherent noise [37,38].

[☆] The review of this paper was arranged by Prof. David W.Walker.

* Corresponding author.

E-mail address: liuzj@iapcm.ac.cn (Z.J. Liu).

Due to the azimuthal symmetry of the system and the property of collisions that leads to the distribution tending to be isotropic, most of the current electrostatic Fokker-Planck codes employ a spectral method, where the distribution function is expanded in the form of Legendre series. Collisions make the series naturally truncated, thus significantly reducing the computational load to describe the full three-dimensional velocity space with only several indices. The electrostatic Fokker-Planck code is first developed by Bell et al. [2] to investigate the electron thermal transport in a large temperature gradient, where the implicit Chang-Copper method [39] and operator splitting method [40] are applied. The electrostatic Fokker-Planck codes have been improved by some other works, including the code developed by Matte and Virmont [41], and the code “SPARK” developed by Epperlein et al. [42] employing alternating-direction implicit method. The Langdon heating term [43] is supplemented in codes “FPI” and “FPI+” [44] to simulate the heating effect caused by inverse bremsstrahlung absorption. The motion of ions described by hydrodynamic equations is supplemented in code “SOL-KiT” developed by Mijin et al. [45]. The spectral method can also expand the distribution function into other series, such as Hermite expansion adopted by Li et al. [46].

To study the kinetic effects of ions, there are also some electrostatic codes where the Fokker-Planck equation is applied to ions while the hydrodynamic equations are applied to electrons, including three 1D2V codes: “FPion” developed by Larroche [47], the code developed by Taitano et al. [48], and “iFP” developed by Taitano et al. [49], where the configuration space in the first and third ones is planar and the second one is spherical. These three codes do not employ spectral methods but instead have two mutually orthogonal velocity grids.

When simulating the collisional plasma with the external laser and magnetostatic field, the system is no longer azimuthal symmetric. The expansion of the Legendre series is invalid. Therefore, it is necessary to develop the electromagnetic Fokker-Planck code. Kingham and Bell developed an electromagnetic Fokker-Planck code “IMPACT” [50] by applying a first-order Cartesian tensor expansion. Then the code “IMPACTA” developed by Thomas et al. [51] where the expansion reaches the second order. Then the code is amended by Nikl et al. [52] to conserve energy. Some codes solve the Fokker-Planck equation without any expansion. For example, the code “FIDO” developed by Sherlock [53] solves the velocity space in the sphere coordinates, while another code developed by Duclous et al. [54] solves the velocity space in Cartesian coordinates. These codes may require tens to hundreds of grids in each coordinate, making them much more inefficient than the codes employing expansions of distribution functions.

In many cases, the laser field and the kinetic effects of electrons and multiple ion species should all be considered. This can be described by the model proposed by Keskinen [55] where the transverse laser electric field is represented by a laser heating term and a ponderomotive term in the Fokker-Planck equation. Therefore, the equations employed by this model are not sufficiently fundamental. Besides, the distribution function is only expanded to the first order, the effects of magnetic fields are not considered, and only the collision terms of the same species appear in the equations.

The spectral method remains an effective approach for solving the electromagnetic Fokker-Planck equation. The distribution function is expanded in spherical harmonics to significantly reduce the computational load. This has been realized by the Fokker-Planck code “KALOS” developed by Bell et al. [56,57] and the improved code “OSHUN” developed by Tzoufras et al. [58]. The Fokker-Planck equation is only applied to electrons while ions are considered as fixed background. The spatial difference scheme employs central difference, which brings about a numerical instability appearing at the location where one of the harmonics of the distribution function is not smooth or varies rapidly, leading to divergence and terminating the calculation. To avoid this numerical instability, the initial distribution needs to be smooth enough, and a large number of grids are desired to resolve the steep interface. Nevertheless, the numerical instability is still severe at the vacuum-plasma interface.

Our work aims to develop a code that meets the following requirements: (i) The code is electromagnetic and applies the Fokker-Planck equation to electrons and multiple ion species. Considering that different species may have significant differences in thermal velocities, each distinct species is assigned a separate velocity grid. (ii) We employ spectral methods that expand the distribution function into a series of spherical harmonics to simulate three-dimensional velocity space and reduce computational load. Furthermore, the calculation scheme should satisfy particle number and energy conservation. To achieve this, we utilize a method that involves discretization followed by correction. (iii) Spherical harmonics can be expanded to any order, allowing for the simulation of highly anisotropic plasmas. (iv) To inhibit the numerical instability, we employ the higher-order total variation diminishing (TVD) scheme, as one of the modern shock-capturing schemes, to deal with the spatial difference [59]. Applying the TVD scheme can also help maintain the positivity of the distribution function even at the vacuum-plasma interface with slight diffusion.

The outline of the paper is as follows. In section 2, we present the required theoretical formulas. In section 3, we give the algorithm of the code, including the derivation of the Fokker-Planck equation for electrons and ions, the discretization expression of each term, the TVD scheme for the spatial difference, and the method to conserve particle number and energy. In section 4, we show simulation results of some typical processes to verify the correctness of the code. The discussion and conclusion are presented in section 5.

2. Physical model

The Fokker-Planck equation for species α is written as

$$\frac{\partial f^\alpha}{\partial t} + \mathbf{v} \cdot \nabla_{\mathbf{r}} f^\alpha + \frac{Z_\alpha e}{m_\alpha} (\mathbf{E} + \mathbf{v} \times \mathbf{B}) \cdot \nabla_{\mathbf{v}} f^\alpha = \sum_{\beta} C(f^\alpha, f^\beta), \quad (1)$$

where α represents electrons or a certain kind of ions in the plasma, $f(\mathbf{r}, \mathbf{v}, t)$ is the velocity distribution function. Z_α and m_α are the charge number and mass of species α , e is the elementary charge, \mathbf{E} is the electrostatic field, and \mathbf{B} is the magnetic field. The Fokker-Planck collision term $C(f^\alpha, f^\beta)$ can be expressed in terms of the Rosenbluth potentials [60]

$$C(f^\alpha, f^\beta) = -\Gamma_{\alpha\beta} \nabla_{\mathbf{v}} \cdot \left(f_\alpha \nabla_{\mathbf{v}} H_{\alpha\beta} - \frac{1}{2} \nabla_{\mathbf{v}} \cdot \nabla_{\mathbf{v}} \nabla_{\mathbf{v}} G_{\alpha\beta} \right), \quad (2)$$

$$H^{\alpha\beta}(\mathbf{v}) = \frac{m_\alpha + m_\beta}{m_\beta} \int d\mathbf{v}' \frac{f^\beta(\mathbf{v}')}{|\mathbf{v} - \mathbf{v}'|}, \quad (3)$$

$$G^{\alpha\beta}(\mathbf{v}) = \int d\mathbf{v}' f^{\beta}(\mathbf{v}') |\mathbf{v} - \mathbf{v}'|. \quad (4)$$

The existence of collisions makes the distribution tend to be isotropic. It is appropriate to expand the distribution function for any species into a convergent series

$$f(\mathbf{v}) = \sum_{l=0}^{\infty} \sum_{m=-l}^l f_l^m(v) P_l^m(\cos\theta) e^{im\phi}, \quad (5)$$

where v , θ and ϕ are spherical coordinates in velocity space and $P_l^m(\cos\theta)$ are the associated Legendre polynomials.

Equation (1) consists of linear and quadratic relations of distribution functions, indicating that the distribution function of each species must be real, which makes Eq. (5) simplified as

$$f(\mathbf{v}) = \sum_{l=0}^{\infty} \sum_{m=-l}^l f_l^m(v) P_l^{|m|}(\cos\theta) e^{im\phi}, \quad f_l^{-m} = (f_l^m)^*. \quad (6)$$

Therefore, only the harmonics with $m \geq 0$ need to be calculated.

Furthermore, for a given distribution $f(\mathbf{v})$, each harmonic can be obtained by

$$f_l^m(v) = \frac{2l+1}{4\pi} \frac{(l-m)!}{(l+m)!} \int f(\mathbf{v}) P_l^m(\cos\theta) e^{-im\phi} \sin\theta d\theta d\phi, \quad m \geq 0, \quad (7)$$

which is useful to obtain the initial condition of each harmonic.

To make normalizations, by substituting $n_{\alpha}/n_e \rightarrow n_{\alpha}$, $m_{\alpha}/m_e \rightarrow M_{\alpha}$, $\omega_{pe}t \rightarrow t$, $v/c \rightarrow v$, $\omega_{pe}x/c \rightarrow x$, $c^3 f/n_e \rightarrow f$, $e\mathbf{E}/m_e c \omega_{pe} \rightarrow \mathbf{E}$ and $e\mathbf{B}/m_e \omega_{pe} \rightarrow \mathbf{B}$, where $\omega_{pe} = \sqrt{n_e e^2 / \epsilon_0 m_e}$ and n_e are the number density (the value is somewhat arbitrary), the kinetic equation of each harmonic is given in Ref. [58]. We modify it to be applicable to multiple species, for species α :

$$\begin{aligned} \frac{\partial (f_{\alpha})_l^m}{\partial t} = & (\mathcal{A}_{\alpha})_l^m + (\mathcal{E}_{\alpha,x})_l^m + (\mathcal{E}_{\alpha,yz})_l^{m=0} + (\mathcal{E}_{\alpha,yz-})_l^{m>0} + (\mathcal{E}_{\alpha,yz+})_l^{m>0} \\ & + (\mathcal{B}_{\alpha,x})_l^m + (\mathcal{B}_{\alpha,yz})_l^{m=0} + (\mathcal{B}_{\alpha,yz+})_l^{m>0} + (\mathcal{B}_{\alpha,yz-})_l^{m>0} + \sum_{\beta} (\mathcal{C}_{\alpha\beta})_l^m. \end{aligned} \quad (8)$$

The linear terms of harmonics are

$$(\mathcal{A}_{\alpha})_l^m = -v \partial_x \left(\frac{l-m}{2l-1} f_{l-1}^m + \frac{l+m+1}{2l+3} f_{l+1}^m \right), \quad (9)$$

$$(\mathcal{E}_{\alpha,x})_l^m = -\frac{Z_{\alpha}}{M_{\alpha}} E_x \left(\frac{l-m}{2l-1} G_{l-1}^m + \frac{l+m+1}{2l+3} H_{l+1}^m \right), \quad (10)$$

$$(\mathcal{E}_{\alpha,yz})_l^{m=0} = \text{Re} \left\{ -\frac{Z_{\alpha}}{M_{\alpha}} (E_y + iE_z) \left[-\frac{l(l-1)}{2l-1} G_{l-1}^1 + \frac{(l+1)(l+2)}{2l+3} H_{l+1}^1 \right] \right\}, \quad (11)$$

$$(\mathcal{E}_{\alpha,yz-})_l^{m>0} = -\frac{Z_{\alpha}}{M_{\alpha}} \frac{E_y - iE_z}{2} \left(\frac{1}{2l-1} G_{l-1}^{m-1} - \frac{1}{2l+3} H_{l+1}^{m-1} \right), \quad (12)$$

$$(\mathcal{E}_{\alpha,yz+})_l^{m>0} = -\frac{Z_{\alpha}}{M_{\alpha}} \frac{E_y + iE_z}{2} \left[-\frac{(l-m)(l-m-1)}{2l-1} G_{l-1}^{m+1} + \frac{(l+m+1)(l+m+2)}{2l+3} H_{l+1}^{m+1} \right], \quad (13)$$

$$(\mathcal{B}_{\alpha,x})_l^m = i \frac{Z_{\alpha}}{M_{\alpha}} m B_x f_l^m, \quad (14)$$

$$(\mathcal{B}_{\alpha,yz})_l^{m=0} = \text{Re} \left\{ -\frac{Z_{\alpha}}{M_{\alpha}} l(l+1) (B_z - iB_y) f_l^1 \right\}, \quad (15)$$

$$(\mathcal{B}_{\alpha,yz+})_l^{m>0} = \frac{Z_{\alpha}}{M_{\alpha}} \frac{B_z + iB_y}{2} f_l^{m-1}, \quad (16)$$

$$(\mathcal{B}_{\alpha,yz-})_l^{m>0} = -\frac{Z_{\alpha}}{M_{\alpha}} \frac{B_z - iB_y}{2} (l-m)(l+m+1) f_l^{m+1}, \quad (17)$$

where $G_l^m = v^l \partial_v (v^{-l} f_l^m)$ and $H_l^m = v^{-l-1} \partial_v (v^{l+1} f_l^m)$. In the numerical method, the ranges of l and m are $l = 0, 1, \dots, l_{\max}$ and $m = 0, 1, \dots, \min(l, m_{\max})$. If l or m is beyond this range, the corresponding f_l^m is zero.

For the isotropic part ($l = m = 0$) of the collision terms, we substitute $(f_{\alpha})_0^0$ to f and $(f_{\beta})_0^0$ to F for brevity (only in the next equation), then $(\mathcal{C}_{\alpha\beta})_0^0$ is given by

$$\begin{aligned} (\mathcal{C}_{\alpha\beta})_0^0 = & \frac{4\pi \Gamma_{\alpha\beta}}{3} \left[\frac{\partial f}{\partial v} \left(\frac{3}{\mu} \frac{1}{v^2} \int_0^v F(u) u^2 du - \frac{1}{v^4} \int_0^v F(u) u^4 du + \frac{2}{v} \int_v^{\infty} F(u) u du \right) \right. \\ & \left. + \frac{\partial^2 f}{\partial v^2} \left(\frac{1}{v^3} \int_0^v F(u) u^4 du + \int_v^{\infty} F(u) u du \right) + \frac{3}{\mu} f F \right], \end{aligned} \quad (18)$$

where $\mu = m_\beta/m_\alpha$. The anisotropic collision term ($l \geq 1$) is the same as Eq. (39) given in Ref. [58].

Maxwell equations are also supplemented to calculate electric and magnetic fields in Eqs. (10)-(17). In 1D configuration space, the fields are naturally decomposed into longitudinal and transverse components. The longitudinal electric field E_x satisfies

$$\frac{\partial E_x}{\partial t} = -\frac{4\pi}{3} \sum_{\alpha} Z_{\alpha} \int_0^{\infty} v^3 f_1^0 dv, \quad (19)$$

while the longitudinal magnetic field does not vary with time and space and is fixed to a constant given at the initial time. To be compatible with the upwind feature of the transverse electromagnetic field, it is modified to its linear combination

$$F_t = [E_y + B_z, E_z - B_y, E_y - B_z, E_z + B_y]. \quad (20)$$

Hence, the transverse electromagnetic field F_t satisfies

$$\begin{aligned} \frac{\partial F_{t1}}{\partial t} + \frac{\partial F_{t1}}{\partial x} &= -\frac{8\pi}{3} \sum_{\alpha} Z_{\alpha} \int_0^{\infty} v^3 \operatorname{Re}\{f_1^1\} dv \\ \frac{\partial F_{t2}}{\partial t} + \frac{\partial F_{t2}}{\partial x} &= \frac{8\pi}{3} \sum_{\alpha} Z_{\alpha} \int_0^{\infty} v^3 \operatorname{Im}\{f_1^1\} dv \\ \frac{\partial F_{t3}}{\partial t} - \frac{\partial F_{t3}}{\partial x} &= -\frac{8\pi}{3} \sum_{\alpha} Z_{\alpha} \int_0^{\infty} v^3 \operatorname{Re}\{f_1^1\} dv \\ \frac{\partial F_{t4}}{\partial t} - \frac{\partial F_{t4}}{\partial x} &= \frac{8\pi}{3} \sum_{\alpha} Z_{\alpha} \int_0^{\infty} v^3 \operatorname{Im}\{f_1^1\} dv. \end{aligned} \quad (21)$$

The linear combination of transverse fields that appear in Eq. (11)-(13) and (15)-(17) can be obtained by simply multiplying a matrix:

$$[E_y + iE_z, E_y - iE_z, B_z + iB_y, B_z - iB_y] = F_t \times \frac{1}{2} \begin{bmatrix} 1 & 1 & 1 & 1 \\ i & -i & -i & i \\ 1 & 1 & -1 & -1 \\ i & -i & i & -i \end{bmatrix}. \quad (22)$$

Sometimes a population of electrons is accelerated to the relativistic velocity. To simulate this relativistic effect, the Fokker-Planck equation for electrons needs to be modified to

$$\frac{\partial f^e}{\partial t} + \frac{\mathbf{p}}{\gamma m_e} \cdot \nabla_r f^e - e \left(\mathbf{E} + \frac{\mathbf{p} \times \mathbf{B}}{\gamma m_e} \right) \cdot \nabla_p f^e = \sum_{\beta} C(f^e, f^{\beta}), \quad (23)$$

where the Lorentz factor is $\gamma = \sqrt{1 + p^2/m_e^2 c^2}$. The suprathermal electrons contribute little to the collision integral, therefore the collision terms remain unchanged.

3. Discretization schemes

3.1. Semi-discrete scheme

The implicit method and operator splitting method are only applicable to solving linear partial differential equations, which requires the code to fix the electric field and the distribution of background particles in collisions within one time step, then they are updated by calculating the solution obtained in the previous step. This process limits the accuracy to $O(\Delta t)$, where Δt is the time step. To prevent potential numerical decay, the code employs the semi-discrete scheme to solve the partial differential equations (8), (19), and (21). Therefore, the code is fully explicit. The discretization of the terms on the right-hand side of these equations is required in x and v space, then an appropriate algorithm for temporal discretization needs to be selected. The accuracy of the second-order Runge-Kutta method is $O(\Delta t^2)$, which is generally sufficient. In our code, the Runge-Kutta methods with different orders are optional for users.

To describe all of the harmonics of the distribution function, the number pairs (l, m) are mapped to a positive integer sequence $llm = 1, 2, \dots, N_{lm}$ as one of the subscripts of the discretized distribution function. The mapping method can be arbitrary. For example, in our code, $l00 = 1$, $l10 = 2$, if $m_{\max} \geq 1$, then $l11 = 3$, $l20 = 4$, $l21 = 5$; or if $m_{\max} = 0$, then $l20 = 3$, $l30 = 4$ and $l40 = 5$, and so on. Once the mapping method is defined, a mapping table is created to realize the conversion between (l, m) to llm . The other two subscripts are $lx = 1, 2, \dots, N_x$ and $lv = 1, 2, \dots, N_v$. The corresponding equally spaced meshes are $x_{lx} = (lx - 1) \times \Delta x$ and $v_{lv} = \Delta v/2 + (lv - 1) \times \Delta v$. Therefore, the distribution harmonics possess three subscripts, and $f_l^m(x, v)$ are discretized as $f_{lx,lv,llm}$.

The next step is to discretize the derivatives ∂_x and ∂_v by central difference and discretize the integral of v by trapezoidal integration. Since spherical harmonics have three indices instead of just one index for a vector, it is necessary to modify the evolution matrix to a multidimensional array. The discretized Eq. (8) can be written as

$$\begin{aligned}
\left(\frac{\partial f_\alpha}{\partial t}\right)_{lx,lv,llm} = & v_{lv,llm} \mathcal{A}_{lx,llm}^{lx0,llm0}(f_\alpha)_{lx0,lv,llm0} + (E_x)_{lx} \mathcal{E}_x^{lv0,llm0}(f_\alpha)_{lx,lv0,llm0} \\
& + \text{Re} \left\{ (E_y + iE_z)_{lx} \mathcal{E}_{yz0}^{lv0,llm0}(f_\alpha)_{lx,lv0,llm0} \right\} \\
& + (E_y - iE_z)_{lx} \mathcal{E}_{yz-}^{lv0,llm0}(f_\alpha)_{lx,lv0,llm0} + (E_y + iE_z)_{lx} \mathcal{E}_{yz+}^{lv0,llm0}(f_\alpha)_{lx,lv0,llm0} \\
& + (B_x)_{lx} \mathcal{B}_x^{llm0}(f_\alpha)_{lx,lv,llm} + \text{Re} \left\{ (B_z - iB_y)_{lx} \mathcal{B}_{yz0}^{llm0}(f_\alpha)_{lx,lv,llm0} \right\} \\
& + (B_z + iB_y)_{lx} \mathcal{B}_{yz+}^{llm0}(f_\alpha)_{lx,lv,llm0} + (B_z - iB_y)_{lx} \mathcal{B}_{yz-}^{llm0}(f_\alpha)_{lx,lv,llm0} \\
& + \sum_{\beta} \left[\mathcal{C}_{\text{Iso}}^{lv1,lv2}(f_\alpha)_{lx,lv1,100}(f_\beta)_{lx,lv2,100} + \mathcal{C}_{\text{Ani},00}^{lv1,lv2}(f_\alpha)_{lx,lv1,100}(f_\beta)_{lx,lv2,llm*} \right. \\
& \left. + \mathcal{C}_{\text{Ani},lm}^{lv1,lv2}(f_\alpha)_{lx,lv1,llm}(f_\beta)_{lx,lv2,100} \right],
\end{aligned} \tag{24}$$

where the repeated indices except lx , lv and llm follow the Einstein summation convention, and the index $llm*$ means the mapping result of (l, m) in mapping table of species β . The multidimensional arrays in Eq. (24) only need to be calculated once before the main iterative loop. The elements of all the multidimensional arrays are presented in Appendix A.

According to the Courant–Friedrichs–Lewy (CFL) stability condition for advection in velocity space, those grids satisfying $lv < l$ should be ignored [58]. Hence, the values in multidimensional arrays with $lv < l$ are zero. Besides, a filtered velocity mesh $v_{lv,llm}$ in the spatial advection term of Eq. (24) is defined as

$$v_{lv,llm} = \begin{cases} v_{lv} & , lv \geq l \\ 0 & , lv < l \end{cases} \tag{25}$$

The product of a multidimensional array and $f_{lx,lv,llm}$ can be calculated efficiently by reshaping them to matrices, multiplying them, and reshaping them back to multidimensional arrays. For example, \mathcal{A} is reshaped into a $(N_x \times N_{lm})$ -by- $(N_{x0} \times N_{lm0})$ matrix and f is reshaped into a $(N_{x0} \times N_{lm0})$ -by- N_v matrix (actually we have $N_{x0} = N_x$ and $N_{lm0} = N_{lm}$, but we distinguish them to distinguish different dimensions of \mathcal{A}). The product of them is a $(N_x \times N_{lm})$ -by- N_v matrix. Finally, we reshape this product into a N_x -by- N_v -by- N_{lm} array. Other products are calculated in the same way. Note that some of these multidimensional arrays, \mathcal{A} , \mathcal{E}_x , \mathcal{E}_{yz0} , \mathcal{E}_{yz+} , and \mathcal{E}_{yz-} , appear to be very large. However, their elements are mostly zero, so they are constructed as sparse matrices in the code.

The introduction of multidimensional arrays aims to realize efficiency calculation, similar to the matrices introduced in Ref. [45], where the distribution function is divided into many one-dimensional arrays at different locations. If there were no third index llm , the advection term would only involve differences about x , while the electric field and collision terms would only involve differences about v . In this case, the multidimensional arrays could be simplified to two-dimensional matrices. However, the third index llm naturally extends the two-dimensional matrices to four-dimensional arrays.

To simulate the relativistic effect, we only need to change the meaning of v_{lv} to discretized momentum $v'_{lv}/\sqrt{1+v'^2_{lv}}$, where v'_{lv} is the discretized velocity that was originally defined. And the advection and magnetic terms in Eq. (24) need to be divided by a factor $\sqrt{1+v'^2_{lv}}$.

3.2. Discretization for collision terms

Firstly we discrete the isotropic part Eq. (18), when v approaches 0, in order to retain accuracy up to $O(v^2)$ (in the code “OSHUN”, it is $O(1)$), the distribution functions are expanded as follows:

$$f = f_0 + f_A v^2 + f_B v^3 + f_C v^4, \tag{26}$$

and

$$F = F_0 + F_A v^2 + F_B v^3 + F_C v^4, \tag{27}$$

where the coefficients can be determined using Cramer's rule with the first four velocity grid points. For the coefficients of f , $f_0 = D_0/D$, $f_A = D_A/D$, $f_B = D_B/D$, $f_C = D_C/D$, and

$$\begin{aligned}
D &= \begin{vmatrix} 1 & v_1^2 & v_1^3 & v_1^4 \\ 1 & v_2^2 & v_2^3 & v_2^4 \\ 1 & v_3^2 & v_3^3 & v_3^4 \\ 1 & v_4^2 & v_4^3 & v_4^4 \end{vmatrix}, D_0 = \begin{vmatrix} f_1 & v_1^2 & v_1^3 & v_1^4 \\ f_2 & v_2^2 & v_2^3 & v_2^4 \\ f_3 & v_3^2 & v_3^3 & v_3^4 \\ f_4 & v_4^2 & v_4^3 & v_4^4 \end{vmatrix}, D_A = \begin{vmatrix} 1 & f_1 & v_1^3 & v_1^4 \\ 1 & f_2 & v_2^3 & v_2^4 \\ 1 & f_3 & v_3^3 & v_3^4 \\ 1 & f_4 & v_4^3 & v_4^4 \end{vmatrix}, \\
D_B &= \begin{vmatrix} 1 & v_1^2 & f_1 & v_1^4 \\ 1 & v_2^2 & f_2 & v_2^4 \\ 1 & v_3^2 & f_3 & v_3^4 \\ 1 & v_4^2 & f_4 & v_4^4 \end{vmatrix}, D_C = \begin{vmatrix} 1 & v_1^2 & v_1^3 & f_1 \\ 1 & v_2^2 & v_2^3 & f_2 \\ 1 & v_3^2 & v_3^3 & f_3 \\ 1 & v_4^2 & v_4^3 & f_4 \end{vmatrix}.
\end{aligned} \tag{28}$$

The coefficients of F can be obtained by replacing the f in the determinants with F , and substituting the first four velocities v_1, v_2, v_3, v_4 with those from the grid corresponding to the species of F . This expansion performs on the condition that the velocity is less than or equal to a given value v_c . Note that the conditions for expanding f and F are different due to their different velocity grids. For instance,

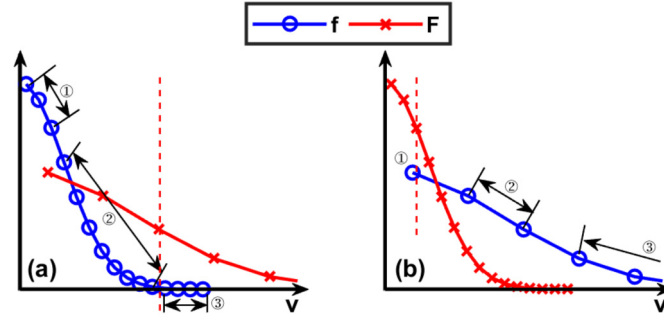


Fig. 1. The expansion of the distribution functions of the scattered particles f and the background particles F in two different situations. The condition for expansion is set to be within three grid points. The marked grid points indicate that (a)① Expand f and F ; (a)② expand F , not expand f ; (a)③ not expand f and F ; (b)① Expand f and F ; (b)② expand f , not expand F ; (b)③ not expand f and F .

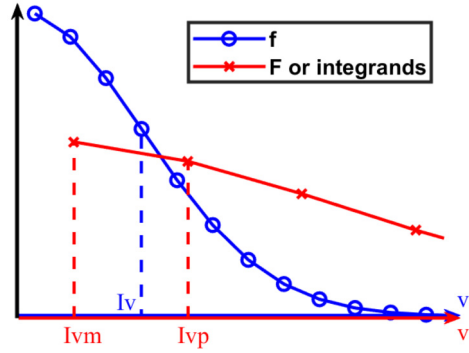


Fig. 2. The schematic diagram of computing the value of F or integrands on the grid of f . The relation between indices I_{vm} , I_{vp} and I_v is illustrated. The x-axis represents the indices of the two velocity grids.

if we expand the first three grid points of f and F , the intervals for expanding and not expanding the distribution functions are shown in Fig. 1.

For the electric field terms, the calculation of $(\mathcal{E}_{\alpha,x})_0^0$ and $(\mathcal{E}_{\alpha,yz})_0^0$ also requires an expansion of the harmonic f_1^0 or f_1^1 for $v \leq v_c$:

$$f = f_A v + f_B v^2 + f_C v^3 + f_D v^4, \quad (29)$$

where f represents f_1^0 or f_1^1 , and the coefficients can also be obtained by Cramer's rule.

It is also necessary to compute the integrals involving F . However, when f and F represent different species, v appearing in the upper or lower limits of the integrals is from the grid of F , while v in the collision terms are from the grid of f . These two often do not coincide. Therefore, it is necessary to perform linear interpolation of v appearing in the integral limits to match the velocity grid of f .

To achieve this, we next specify that v and v^* are the velocity grids of f and F . Then we define v_p^* as the smallest grid point that satisfies $v_p^* \geq v$, and v_m^* as the largest grid point that satisfies $v_m^* \leq v$. And we define $v_{lp}^* = v_p^*$ and $v_{lm}^* = v_m^*$. The relation between I_v , I_{vp} and I_{vm} is shown in Fig. 2. For integrals where the velocity appears in the lower limits, the interpolated integrand $P_{\text{interp},lo}$ (which is also $F(u)u$ in Eq. (18)) is given by

$$P_{\text{interp},lo} = \frac{1}{\Delta v^*} \left[(v_{lp}^* - v) P_{I_{vp}-1} + (v - v_{lp}^*) P_{I_{vp}} \right], \quad v > v_1^*, \quad (30)$$

and

$$P_{\text{interp},lo} = \frac{v}{v_1^*} F_1, \quad v \leq v_1^*. \quad (31)$$

For integrals that v appears in the upper limits, the integrand $P_{\text{interp},up}$ (which can be $F(u)u^2$ or $F(u)u^4$ in Eq. (18)) is given by

$$P_{\text{interp},up} = \frac{1}{\Delta v^*} \left[(v_{lm}^* - v) P_{I_{vm}} + (v - v_{lm}^*) P_{I_{vm}+1} \right], \quad v < v_{Nv}^*, \quad (32)$$

when $v \geq v_{Nv}^*$, the integrals equal to zero, we do not need interpolation.

Besides, the term fF in Eq. (18) implies that the value of F need to be expressed on the grid of f by means of interpolation (see Fig. 2). Therefore, when the velocity is v in the grid of f , the value of $F(v)$ is given by

$$\begin{aligned} F(v) &= \frac{1}{\Delta v^*} \left[(v_{lm}^* - v) F_{I_{vm}} + (v - v_{lm}^*) F_{I_{vm}+1} \right], \text{ for } I_{vc}^* < I_{vm} \text{ and } v < v_{Nv}^*, \\ F(v) &= F_0 + F_A v^2 + F_B v^3 + F_C v^4, \text{ for } I_{vm} \leq I_{vc}^* \text{ or } I_{vm} \text{ does not exist,} \\ F(v) &= 0, \text{ for } v \geq v_{Nv}^*, \end{aligned} \quad (33)$$

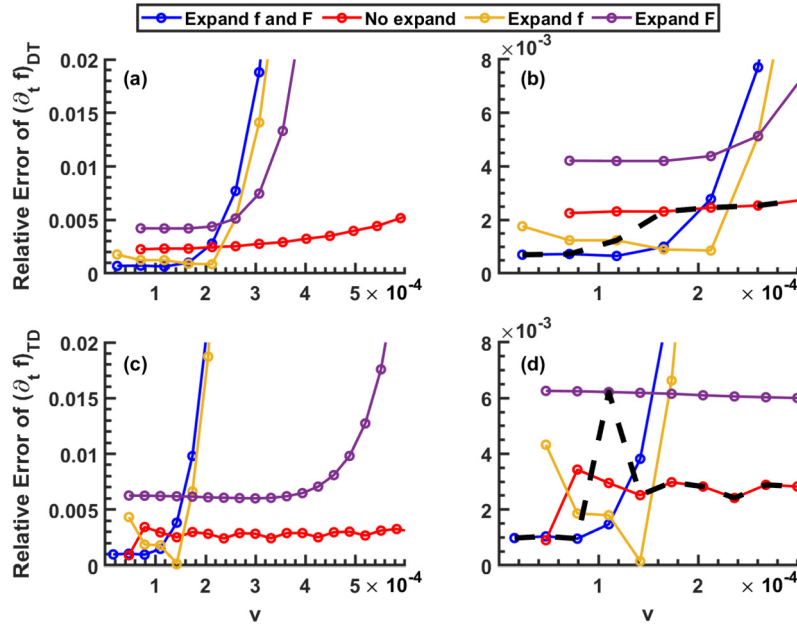


Fig. 3. The relative error of the collision term for the DT plasma calculated by different expansion methods. (a)(b) The results for DT collision term. (c)(d) The results for TD collision term. The black dashed lines in (b) and (d) represent the result for $lvc_D = lvc_T = 3$.

where $v_{lvc*}^* = v_c^*$. The usual choice in this work for lvc is 3.

To demonstrate the performance of this discretized equation, we calculate the isotropic part of ion collision terms $(C_{DT})_0^0$ and $(C_{TD})_0^0$ in a deuterium-tritium plasma, where the D and T ions follow Maxwellian distributions with temperatures of 150 eV and 100 eV, respectively, and the ratio of number densities is 1 : 1. Fig. 3(a)(b) displays the relative error of the DT collision term $(C_{DT})_0^0$ under different expansion schemes. In Fig. 3(b), the black dashed line represents result for $lvc_D = lvc_T = 3$. Fig. 3(c)(d) displays the same results for TD collision. It can be seen that the relative error is in the order of 10^{-3} .

The discretization method for anisotropic collision terms is similar to isotropic collisions, except that there is no need to expand the distribution for $v \leq v_c$ to achieve good accuracy.

The error of the trapezoidal integration can be expressed as

$$\epsilon_{\text{trapz}} \leq \frac{v_{\text{up}} - v_{\text{lo}}}{12} \Delta v^* \max_{v_{\text{up}} \leq v \leq v_{\text{lo}}} P(v), \quad (34)$$

which is of order $O(\Delta v^*)$. To estimate the error of the interpolation, we expand $F(v)$ as

$$\begin{aligned} F(v) &= F_{lvm} + F'(v_{lvm}^*)(v - v_{lvm}^*) + \frac{1}{2} F''(v_{lvm}^*)(v - v_{lvm}^*)^2 + \dots \\ F(v) &= F_{lvm+1} + F'(v_{lvm+1}^*)(v - v_{lvm+1}^*) + \frac{1}{2} F''(v_{lvm+1}^*)(v - v_{lvm+1}^*)^2 + \dots \end{aligned} \quad (35)$$

By substituting it into the first equation from Eq. (33), the leading order of the error of interpolation is given by

$$\epsilon_{\text{interp}} = F(v) - F_{\text{interp}}(v) \approx \frac{(v_{lvm+1}^* - v)(v - v_{lvm}^*)}{\Delta v^*} (F'(v_{lvm+1}^*) - F'(v_{lvm}^*)). \quad (36)$$

Note that $(v_{lvm+1}^* - v)(v - v_{lvm}^*) \leq \Delta v^*/4$ and $F'(v_{lvm+1}^*) - F'(v_{lvm}^*) \approx F''(v) \Delta v^*$ yield

$$\epsilon_{\text{interp}} \leq \frac{1}{4} F''(v) \Delta v^{*2}, \quad (37)$$

which is also of order $O(\Delta v^{*2})$. Consequently, the total error of the discretization of the collision terms is of order $\sum_{\beta} O(\Delta v_{\beta}^2)$.

3.3. Discretization for Maxwell equations

The equations of discretized electric and magnetic fields are given by

$$\frac{\partial E_x}{\partial t} = - \sum_{\alpha} \mathcal{J}_{x,\alpha}^{lv0} (f_{\alpha})_{lx,lv0,l10}, \quad (38)$$

and

$$\left(\frac{\partial F_{t1}}{\partial t} \right)_{lx} = -S_r^{lx0} F_{t1}^{lx0} + \mathcal{L}_I(t)_{lx} - \sum_{\alpha} \text{Re} \left\{ \mathcal{J}_{y,\alpha}^{lv0} (f_{\alpha})_{lx,lv0,l11} \right\}$$

$$\begin{aligned}
\left(\frac{\partial F_{t2}}{\partial t}\right)_{lx} &= -S_{r,lx}^{lx0} F_{t2,lx0} + \mathcal{L}_l(t)_{lx} - \sum_{\alpha} \text{Im} \left\{ \mathcal{J}_{z,\alpha}^{lv0} (f_{\alpha})_{lx,lv0,l11} \right\} \\
\left(\frac{\partial F_{t3}}{\partial t}\right)_{lx} &= S_{l,lx}^{lx0} F_{t3,lx0} + \mathcal{L}_r(t)_{lx} - \sum_{\alpha} \text{Re} \left\{ \mathcal{J}_{y,\alpha}^{lv0} (f_{\alpha})_{lx,lv0,l11} \right\} \\
\left(\frac{\partial F_{t4}}{\partial t}\right)_{lx} &= S_{l,lx}^{lx0} F_{t4,lx0} + \mathcal{L}_r(t)_{lx} - \sum_{\alpha} \text{Im} \left\{ \mathcal{J}_{z,\alpha}^{lv0} (f_{\alpha})_{lx,lv0,l11} \right\},
\end{aligned} \tag{39}$$

where $S_{r,l}$ represent spacial difference matrices about right and left propagation, and $\mathcal{L}_{l,r}(t)$ are related to incident laser lights from left and right boundaries.

3.4. TVD scheme for the spatial difference in advection term

When the central difference for the spatial difference in advection term is applied, numerical instability occurs in the regions of steep density, rarefied plasma-vacuum interface, and non-periodic boundary conditions. If the instability is not handled properly, the non-physical fluctuation appears and grows exponentially, which would terminate the program. Therefore, it is necessary to implement the TVD scheme.

The advection term can be regarded as a system of N_{lm} hyperbolic equations

$$\mathcal{A}(x, t)_{llm} + v A_{llm}^{llm0} \frac{\partial f(x, t)_{llm}}{\partial x} = 0, \tag{40}$$

by defining a matrix A whose elements are

$$A_{llm}^{llm0} = \frac{l-m}{2l-1} \delta_{l(l-1)m}^{llm0} + \frac{l+m+1}{2l+3} \delta_{l(l+1)m}^{llm0}. \tag{41}$$

It can be decomposed into $A = R\Lambda L$ with $\Lambda = \text{diag}(a_1, a_2, \dots, a_{N_{lm}})$, $R = [\mathbf{r}_1, \mathbf{r}_2, \dots, \mathbf{r}_{N_{lm}}]$, and $L = [\mathbf{l}_1, \mathbf{l}_2, \dots, \mathbf{l}_{N_{lm}}]^T$, where a_k , \mathbf{r}_k and \mathbf{l}_k are the eigenvalues, right and left eigenvectors of A , respectively. By applying the second-order symmetrical algorithm of Yee [59], the modified discretized advection term is given by

$$\begin{aligned}
\mathcal{A}_{lx,lv,llm} &= -v_{lv,llm} \mathcal{A}_{lx,llm}^{lx0,llm0} f_{lx0,lv,llm0} \\
&+ \frac{v_{lx,llm}}{2\Delta x} L_k^{llm0} |a_k| R_{llm}^k (f_{lx+1,lv,llm0} - 2f_{lx,lv,llm0} + f_{lx-1,lv,llm0}) \\
&- \frac{v_{lx,llm}}{2\Delta x} \left[\min \text{mod} \begin{pmatrix} L_k^{llm0} (f_{lx,lv,llm0} - f_{lx-1,lv,llm0}) \\ L_k^{llm0} (f_{lx+1,lv,llm0} - f_{lx,lv,llm0}) \\ L_k^{llm0} (f_{lx+2,lv,llm0} - f_{lx+1,lv,llm0}) \end{pmatrix} \right. \\
&\quad \left. - \min \text{mod} \begin{pmatrix} L_k^{llm0} (f_{lx-1,lv,llm0} - f_{lx-2,lv,llm0}) \\ L_k^{llm0} (f_{lx,lv,llm0} - f_{lx-1,lv,llm0}) \\ L_k^{llm0} (f_{lx+1,lv,llm0} - f_{lx,lv,llm0}) \end{pmatrix} \right] |a_k| R_{llm}^k,
\end{aligned} \tag{42}$$

where the “min mod” function is

$$\min \text{mod} \begin{pmatrix} a \\ b \\ c \end{pmatrix} = \begin{cases} \text{sgn}(a) \times \min(|a|, |b|, |c|), & a, b \text{ and } c \text{ is of the same sign} \\ 0, & \text{otherwise} \end{cases}. \tag{43}$$

The TVD scheme also matters in regions with smooth density. It helps inhibit negative values of the distribution functions throughout the simulation. In the simulations of Ref. [58], where central difference is applied, extra terms are usually added to the initial distributions to maintain the positivity of the distribution function. These terms are non-physical, and it is also inconvenient to determine their specific expressions. For these reasons, it is recommended to apply the TVD scheme in many cases.

The discretized equation (42) needs to be calculated efficiently. It can be noticed that Eq. (42) can be divided into three terms. The first term is exactly the discretized equation for the advection term given by the central difference. The second term has a linear relationship with the distribution function and can also be written as a multidimensional array multiplied by the distribution function. And it also consists of a factor of velocity $v_{lv,llm}$. Thus, the second term can be combined with the first term after computing the matrix formed by the eigenvectors and eigenvalues, making it to an expression of $-v_{lv,llm} \mathcal{A}_{lx,llm}^{lx0,llm0} f_{lx0,lv,llm0}$. As for the third term, it cannot be written as a product of multidimensional arrays, but an alternative approach can be designed for its efficient computation: The third term can be written as $-v_{lv,llm} \mathcal{M}_{lx,lv,k} R_{llm}^k$, where

$$\mathcal{M}_{lx,lv,k} = |a_k| \times \left[\min \text{mod} \begin{pmatrix} L_k^{llm0} (f_{lx,lv,llm0} - f_{lx-1,lv,llm0}) \\ L_k^{llm0} (f_{lx+1,lv,llm0} - f_{lx,lv,llm0}) \\ L_k^{llm0} (f_{lx+2,lv,llm0} - f_{lx+1,lv,llm0}) \end{pmatrix} - \min \text{mod} \begin{pmatrix} L_k^{llm0} (f_{lx-1,lv,llm0} - f_{lx-2,lv,llm0}) \\ L_k^{llm0} (f_{lx,lv,llm0} - f_{lx-1,lv,llm0}) \\ L_k^{llm0} (f_{lx+1,lv,llm0} - f_{lx,lv,llm0}) \end{pmatrix} \right]. \tag{44}$$

Four different spatial differences of distribution function appear in Eq. (44). We define

$$\begin{aligned}\mathcal{H}^{-}_{lx,lv,k} &= |a_k| L_k^{lm0} (f_{lx-1,lv,lm0} - f_{lx-2,lv,lm0}), \\ \mathcal{H}_{lx,lv,k} &= |a_k| L_k^{lm0} (f_{lx,lv,lm0} - f_{lx-1,lv,lm0}), \\ \mathcal{H}^{+}_{lx,lv,k} &= |a_k| L_k^{lm0} (f_{lx+1,lv,lm0} - f_{lx,lv,lm0}), \\ \mathcal{H}^{++}_{lx,lv,k} &= |a_k| L_k^{lm0} (f_{lx+2,lv,lm0} - f_{lx+1,lv,lm0}).\end{aligned}$$

To calculate each spatial difference only once, we can define

$$\overline{\mathcal{H}}_{lx,lv,k} = |a_k| L_k^{lm0} (f_{lx-1,lv,lm0} - f_{lx-2,lv,lm0}), \quad (45)$$

where the range of lx is $1, 2, \dots, N_x + 3$. This is a multidimensional array of size $(N_x + 3) \times N_v \times N_{lm}$. When the subscript lx of the distribution function exceeds the boundary of 1 to N_x , its value is determined by the boundary conditions. For example, when lx exceeds the range, f_{lx} takes the value of $f_{lx \pm N_x}$ under periodic boundary conditions, and f_{lx} is set to 0 under vacuum boundary conditions. By calculating $\overline{\mathcal{H}}$, relevant segments can be extracted to obtain \mathcal{H}^{-} , \mathcal{H} , \mathcal{H}^{+} , and \mathcal{H}^{++} , i.e.,

$$\begin{aligned}\mathcal{H}^{-}_{lx,lv,k} &= \overline{\mathcal{H}}_{lx,lv,k}, \\ \mathcal{H}_{lx,lv,k} &= \overline{\mathcal{H}}_{lx+1,lv,k}, \\ \mathcal{H}^{+}_{lx,lv,k} &= \overline{\mathcal{H}}_{lx+2,lv,k}, \\ \mathcal{H}^{++}_{lx,lv,k} &= \overline{\mathcal{H}}_{lx+3,lv,k}.\end{aligned} \quad (46)$$

Next, we need to find a way to express \mathcal{M} with $\overline{\mathcal{H}}$. The efficiency of the computation requires that this expression involves only array-wise operations, i.e., it should not contain any subscripts like lx . Upon observation, it is found that in Eq. (44), the two “min mod” functions being subtracted each have two identical terms. It can be proved that for any constants a , b , c , and d , the following identity holds:

$$\begin{aligned}\min \text{mod}(a, b, c) - \min \text{mod}(a, b, d) &= \delta_{\text{sgn}(a)}^{\text{sgn}(b)} \text{sgn}(a) \\ &\times \left[\delta_{\text{sgn}(a)}^{\text{sgn}(c)} \min \{|a|, |b|, |c|\} - \delta_{\text{sgn}(a)}^{\text{sgn}(d)} \min \{|a|, |b|, |d|\} \right],\end{aligned} \quad (47)$$

where “sgn” is the sign function. Utilizing this relationship, the relation between \mathcal{M} and $\overline{\mathcal{H}}$ can be written as

$$\begin{aligned}\mathcal{M} &= \delta(\text{sgn}(\mathcal{H}), \text{sgn}(\mathcal{H}^{+})) \circ \text{sgn}(\mathcal{H}) \\ &\circ \left[\delta(\text{sgn}(\mathcal{H}), \text{sgn}(\mathcal{H}^{++})) \circ \min_4 \left\{ \text{cat}(|\mathcal{H}|, |\mathcal{H}^{+}|, |\mathcal{H}^{++}|) \right\} \right. \\ &\quad \left. - \delta(\text{sgn}(\mathcal{H}), \text{sgn}(\mathcal{H}^{-})) \circ \min_4 \left\{ \text{cat}(|\mathcal{H}|, |\mathcal{H}^{+}|, |\mathcal{H}^{-}|) \right\} \right],\end{aligned} \quad (48)$$

where the binary symbol δ represents comparing two arrays element-wise and outputs a new array with elements being 1 when the corresponding elements of the two input arrays are equal, and being 0 otherwise. The binary symbol “ \circ ” denotes element-wise multiplication of arrays (Hadamard product). The symbol “ cat ” concatenates all the arrays in its arguments along the 4th dimension, resulting in three $N_x \times N_v \times N_{lm}$ arrays being concatenated into one $N_x \times N_v \times N_{lm} \times 3$ array. The unary symbol “ \min_4 ” computes the minimum value along the 4th dimension of an array, transforming an $N_x \times N_v \times N_{lm} \times 3$ array into an $N_x \times N_v \times N_{lm} \times 1$ array. All these operation relationships are array-wise, enabling efficient computation in mature programming languages.

The process of calculating the TVD scheme can be summarized as follows: First, for the first two terms, the multidimensional array \mathcal{A} obtained from the central difference scheme is corrected to $\overline{\mathcal{A}}$. Then, for the third term, $\overline{\mathcal{H}}$ is obtained by Eq. (45). Like other multidimensional arrays, it only needs to be calculated once. Next, \mathcal{M} is calculated successively by Eqs. (46) and (48). Finally, the result for the third term is obtained by multidimensional array multiplication $-v_{lv,lm} \mathcal{M}_{lx,lv,k} R_{lm}^k$.

By employing this algorithm, the time consumption for advection term calculations of the TVD scheme is approximately three to four times that of the central difference. Nevertheless, the calculation time is mainly consumed in computing the collision term. Thus the total calculation time is slightly affected when the TVD scheme is implemented in simulating collisional plasmas.

To show the performance of the TVD scheme, a simple diffusion process of a collisionless plasma with step initial density is simulated. The length of configuration space is $8 c/\omega_{pe}$, resolved with 64 x -cells ($\Delta x = 0.127 c/\omega_{pe}$). The temperature of electrons is 300 eV. The maximum value in electron velocity space is 10 times of the thermal velocity and is resolved by 80 v -cells ($\Delta v = 0.003 c$). For electrons, we set $l_{\max} = 7$, $m_{\max} = 0$, and we set $l_{\max} = m_{\max} = 0$ for fixed ions. The time step is $\Delta t = 0.01$. The density profile is shown in Fig. 4(a). The density profile at $\omega_{pe} t = 20$ of different difference schemes is shown in Fig. 4(b), and the simulation results of the distribution function in the vacuum near the vacuum-plasma interface ($x = 3 c/\omega_{pe}$) of different difference schemes are shown in Fig. 4(c)(d), respectively. It can be seen that the TVD scheme effectively avoids numerical instability.

3.5. Modification by particle number and energy conservation

The normalized number N_α and energy E_α of species α is given by

$$N_\alpha = 4\pi \iint (f_\alpha)_0^0(v) v^2 dv dx, \quad (49)$$

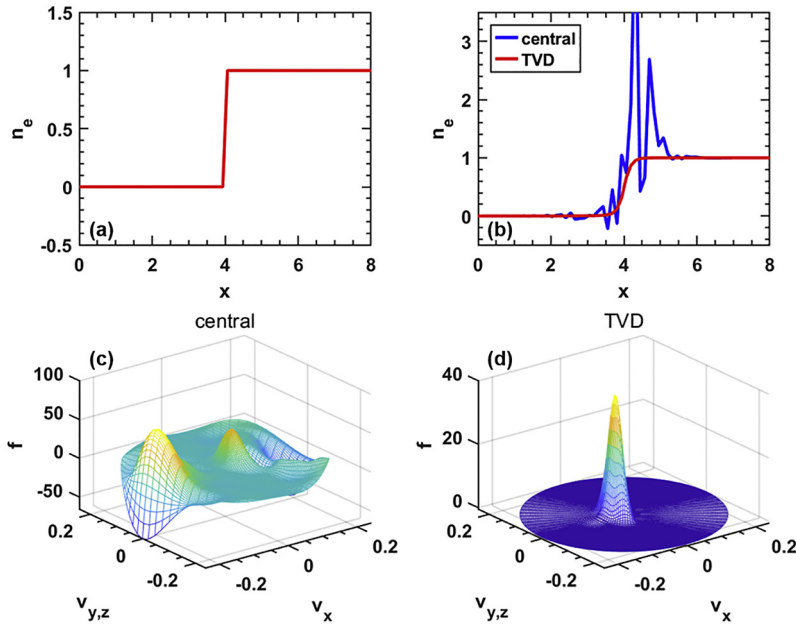


Fig. 4. Comparison between the central difference and TVD Scheme at $\omega_{pet} = 20$. After a certain simulation time, the numerical instability of the central difference results in overflow and terminates the program. (a) The initial density profile. The vacuum is on the left side of $x = 4$, where there is a sudden jump to a uniform plasma on the right side. (b) Density profile at $\omega_{pet} = 20$. The solid blue line represents the simulation results of the central difference, and the solid red line represents the simulation results of the TVD scheme. (c) Distribution function at $\omega_{pet} = 20$ and position $\omega_{pe}x/c = 3$ obtained by the central difference. (d) Distribution function at $\omega_{pet} = 20$ and position $\omega_{pe}x/c = 3$ obtained by TVD scheme. (For interpretation of the colors in the figure(s), the reader is referred to the web version of this article.)

and

$$E_\alpha = 2\pi m_\alpha \iint (f_\alpha)_0^0(v) v^4 dv dx. \quad (50)$$

By discretization, the conservation laws $\partial N_\alpha / \partial t = 0$ and $\partial E_\alpha / \partial t = 0$ yield

$$4\pi \sum_{lx0} \Delta x \sum_{lv0} r_{lv0} \left(\frac{\partial f_\alpha}{\partial t} \right)_{lx0,lv0,100} v_{\alpha,lv0}^2 \Delta v_\alpha = 0, \quad (51)$$

and

$$2\pi m_\alpha \sum_{lx0} \Delta x \sum_{lv0} r_{lv0} \left(\frac{\partial f_\alpha}{\partial t} \right)_{lx0,lv0,100} v_{\alpha,lv0}^4 \Delta v_\alpha = 0, \quad (52)$$

where

$$r_{lv0} = \begin{cases} 0.75, & lv0 = 1 \\ 0.5, & lv0 = N_v \\ 1, & 1 < lv0 < N_v \end{cases}$$

is the coefficient of the trapezoidal integral.

From Eq. (42), it can be easily observed that $\sum_{lx0} \mathcal{A}_{lx0,lv0,100} = 0$, thereby we can obtain

$$4\pi \sum_{lx0} \Delta x \sum_{lv0} r_{lv0} \mathcal{A}_{lx0,lv0,100} v_{\alpha,lv0}^2 \Delta v_\alpha = 0, \quad (53)$$

and

$$2\pi m_\alpha \sum_{lx0} \Delta x \sum_{lv0} r_{lv0} \mathcal{A}_{lx0,lv0,100} v_{\alpha,lv0}^4 \Delta v_\alpha = 0, \quad (54)$$

i.e., the discretized equation of the TVD scheme (42) satisfies conservation of particle number and energy.

Magnetic field terms do not affect conservation properties, as they only impact harmonics with $l \geq 1$. Other terms, if not modified, cannot satisfy the required conservation of particle number and energy. Therefore, the electric field terms and collision terms need to be modified to formats that conserve the particle number. Moreover, isotropic collision terms between the same species should conserve energy for this species, while isotropic collision terms between different species should conserve the total energy.

To achieve this, the modified terms need to minimize the sum of the squared differences from the unmodified terms. We first modify the isotropic collision terms between the same species. For simplicity, $(C_{\alpha\alpha})_{lx,lv,100}$ is simplified as C_{lv} , as collision terms does not contain x , and α is omitted. We define C_{lv} and \tilde{C}_{lv} as modified and unmodified terms, then calculate the minimum value of $\sum_{lv0} (C_{lv}/\tilde{C}_{lv0} - 1)^2$ under constraints $\sum_{lv0} r_{lv0} v_{lv0}^2 C_{lv} = 0$ and $\sum_{lv0} r_{lv0} v_{lv0}^4 C_{lv} = 0$, utilizing Lagrange multiplier method, the Lagrangian function is given by

$$L(C_1, C_2, \dots, C_{N_V}; \lambda_N, \lambda_E) = \sum_{Iv0} \left(\frac{C_{Iv0}}{\tilde{C}_{Iv0}} - 1 \right)^2 + \lambda_N \sum_{Iv0} r_{Iv0} v_{Iv0}^2 C_{Iv0} + \lambda_E \sum_{Iv0} r_{Iv0} v_{Iv0}^4 C_{Iv0}. \quad (55)$$

Solving the equations $\partial L / \partial C_{Iv} = 0$, $Iv = 1, 2, \dots, N_V$ and the two constraints yields

$$C_{Iv} = \tilde{C}_{Iv} - \frac{1}{2} \tilde{C}_{Iv}^2 r_{Iv} v_{Iv}^2 (\lambda_N + v_{Iv}^2 \lambda_E), \quad (56)$$

where λ_N and λ_E can be obtained by solving equations

$$\begin{aligned} \frac{1}{2} \sum_{Iv0} (r_{Iv0}^2 v_{Iv0}^4 \tilde{C}_{Iv0}^2) \lambda_N + \frac{1}{2} \sum_{Iv0} (r_{Iv0}^2 v_{Iv0}^6 \tilde{C}_{Iv0}^2) \lambda_E &= \sum_{Iv0} (r_{Iv0} v_{Iv0}^2 \tilde{C}_{Iv0}) \\ \frac{1}{2} \sum_{Iv0} (r_{Iv0}^2 v_{Iv0}^6 \tilde{C}_{Iv0}^2) \lambda_N + \frac{1}{2} \sum_{Iv0} (r_{Iv0}^2 v_{Iv0}^8 \tilde{C}_{Iv0}^2) \lambda_E &= \sum_{Iv0} (r_{Iv0} v_{Iv0}^4 \tilde{C}_{Iv0}). \end{aligned} \quad (57)$$

By using the same approach, isotropic collision terms for different species can be modified to follow particle number conservation and total energy conservation. For the sake of simplicity and distinction, we use C_{Iv} and C_{Iv}^* to represent $(C_{\alpha\beta})_{Ix,Iv,100}$ and $(C_{\beta\alpha})_{Ix,Iv,100}$, respectively. An asterisk (*) added to m , r , Δv and v indicates quantities belonging to species β , whereas no asterisk indicates those belonging to species α . The constraints are $4\pi \Delta v \sum_{Iv1} r_{Iv1} v_{Iv1}^2 C_{Iv1} = 0$, $4\pi \Delta v^* \sum_{Iv2} r_{Iv2}^* v_{Iv2}^{*2} C_{Iv1}^* = 0$, and $2\pi m \Delta v \sum_{Iv1} r_{Iv1} v_{Iv1}^4 C_{Iv1} + 2\pi m^* \Delta v^* \sum_{Iv2} r_{Iv2}^* v_{Iv2}^{*4} C_{Iv2}^* = 0$. The minimum value of $\sum_{Iv1} (C_{Iv1} / \tilde{C}_{Iv1} - 1)^2 + \sum_{Iv2} (C_{Iv2}^* / \tilde{C}_{Iv2}^* - 1)^2$ is required. The Lagrangian function is given by

$$\begin{aligned} L(C_1, C_2, \dots, C_{N_{V1}}; C_1^*, C_2^*, \dots, C_{N_{V2}}^*; \lambda_{N1}, \lambda_{N2}, \lambda_E) &= \sum_{Iv1} \left(\frac{C_{Iv1}}{\tilde{C}_{Iv1}} - 1 \right)^2 + \sum_{Iv2} \left(\frac{C_{Iv2}^*}{\tilde{C}_{Iv2}^*} - 1 \right)^2 \\ &+ \lambda_{N1} \left(4\pi \Delta v \sum_{Iv1} r_{Iv1} v_{Iv1}^2 C_{Iv1} \right) + \lambda_{N2} \left(4\pi \Delta v^* \sum_{Iv2} r_{Iv2}^* v_{Iv2}^{*2} C_{Iv1}^* \right) \\ &+ \lambda_E \left(2\pi m \Delta v \sum_{Iv1} r_{Iv1} v_{Iv1}^4 C_{Iv1} + 2\pi m^* \Delta v^* \sum_{Iv2} r_{Iv2}^* v_{Iv2}^{*4} C_{Iv2}^* \right). \end{aligned} \quad (58)$$

Solving the equations $\partial L / \partial C_{Iv} = 0$, $Iv = 1, 2, \dots, N_{V1}$, $\partial L / \partial C_{Iv}^* = 0$, $Iv = 1, 2, \dots, N_{V2}$ and the three constraints yields

$$\begin{aligned} C_{Iv} &= \tilde{C}_{Iv} - 2\pi \lambda_{N1} \Delta v \tilde{C}_{Iv}^2 r_{Iv} v_{Iv}^2 - \pi \lambda_E m \Delta v \tilde{C}_{Iv}^2 r_{Iv} v_{Iv}^4 \\ C_{Iv}^* &= \tilde{C}_{Iv}^* - 2\pi \lambda_{N2} \Delta v^* \tilde{C}_{Iv}^{*2} r_{Iv}^* v_{Iv}^{*2} - \pi \lambda_E m^* \Delta v^* \tilde{C}_{Iv}^{*2} r_{Iv}^* v_{Iv}^{*4}. \end{aligned} \quad (59)$$

The Lagrange multipliers λ_{N1} , λ_{N2} and λ_E can be obtained by solving equations

$$A \begin{bmatrix} \lambda_{N1} \\ \lambda_{N2} \\ \lambda_E \end{bmatrix} = B, \quad (60)$$

where the elements are

$$\begin{aligned} A_{11} &= 2\pi \Delta v^2 \sum_{Iv1} (r_{Iv1}^2 v_{Iv1}^4 \tilde{C}_{Iv1}^2), \\ A_{12} &= A_{21} = 0, \\ A_{13} &= A_{31} = \pi \Delta v^2 m \sum_{Iv1} (r_{Iv1}^2 v_{Iv1}^6 \tilde{C}_{Iv1}^2), \\ A_{22} &= 2\pi \Delta v^{*2} \sum_{Iv2} (r_{Iv2}^{*2} v_{Iv2}^{*4} \tilde{C}_{Iv2}^{*2}), \\ A_{23} &= A_{32} = \pi \Delta v^{*2} m^* \sum_{Iv2} (r_{Iv2}^{*2} v_{Iv2}^{*6} \tilde{C}_{Iv2}^{*2}), \\ A_{33} &= \frac{1}{2} m^2 \Delta v^2 \sum_{Iv1} (r_{Iv1}^2 v_{Iv1}^8 \tilde{C}_{Iv1}^2) + \frac{1}{2} m^{*2} \Delta v^{*2} \sum_{Iv2} (r_{Iv2}^{*2} v_{Iv2}^{*8} \tilde{C}_{Iv2}^{*2}), \\ B_1 &= \Delta v \sum_{Iv1} (r_{Iv1} v_{Iv1}^2 \tilde{C}_{Iv1}), \\ B_2 &= \Delta v^* \sum_{Iv2} (r_{Iv2}^* v_{Iv2}^{*2} \tilde{C}_{Iv2}^*), \\ B_3 &= \frac{1}{2} m \Delta v \sum_{Iv1} (r_{Iv1} v_{Iv1}^4 \tilde{C}_{Iv1}) + \frac{1}{2} m^* \Delta v^* \sum_{Iv2} (r_{Iv2}^* v_{Iv2}^{*4} \tilde{C}_{Iv2}^*). \end{aligned} \quad (61)$$

In our code, we assume that ions remain stationary during electron-ion collision processes, and there is no energy exchange in the electron-ion collision term. Therefore, energy conservation modification is not applied when calculating ion-electron collision terms. As a result, a small amount of energy loss occurs when considering ion-electron collisions. Additionally, the semi-anisotropic approximation [61] in the physical model leads to the non-conservation of momentum. Therefore, although it is possible to modify the code to conserve momentum, this is not implemented.

The isotropic parts of the electric field terms $(\mathcal{E}_{\alpha,x})_0^0$ and $(\mathcal{E}_{\alpha,yz})_0^0$ also require particle number conservation modification. Denoting them as $\tilde{\mathcal{E}}_{1v}$ before modification, the modified electric field terms are given by

$$\mathcal{E}_{1v} = \tilde{\mathcal{E}}_{1v} - \frac{\sum_{1v0} (r_{1v0} v_{1v0}^2 \tilde{\mathcal{E}}_{1v0})}{\sum_{1v0} (r_{1v0}^2 v_{1v0}^4 \tilde{\mathcal{E}}_{1v0}^2)} \tilde{\mathcal{E}}_{1v}^2 r_{1v} v_{1v}^2. \quad (62)$$

4. Simulations

4.1. Two-stream instability

To demonstrate the effect of the TVD scheme and benchmark the advection term and longitudinal electric field term, the initial conditions are set as two beams of electrons with opposite directions to simulate the two-stream instability in a collisionless plasma. The distribution function is expressed as

$$\begin{aligned} f_0^0(t=0) &= A_0 \exp \left[\frac{(p - p_d)^2}{2m_e v_T^2} \right], \\ f_1^0(t=0) &= -A_0 A_{\text{noise}} \exp \left[\frac{(p - p_d)^2}{2m_e v_T^2} \right] \sin \left(\frac{2\pi x}{L} \right), \\ f_2^0(t=0) &= 2A_0 \left[\frac{(p - p_d)^2}{2m_e v_T^2} \right]. \end{aligned} \quad (63)$$

The momentum of each beam is mainly concentrated around $p_d = 0.5 m_e c$. The electron thermal velocity is approximately $v_T \approx 0.1084 c$, corresponding to an electron temperature of $T_e = 6$ keV. The simulation length is $L = 10 c/\omega_{pe}$. The parameter A_0 is a normalization constant determined by the built-in functionality, and the parameter $A_{\text{noise}} = 0.02$ represents the initial perturbation amplitude. This distribution function is equivalent to

$$f \propto \exp \left[\frac{(p - p_d)^2}{2m_e v_T^2} \right] \cos^2 \theta. \quad (64)$$

Other parameters are set as follows: $N_x = 128$, $\Delta t = 0.02$. For electrons, $N_v = 96$, $v_{\text{max}} = 1.8 c$, $l_{\text{max}} = 15$, $m_{\text{max}} = 0$. For fixed ions, $l_{\text{max}} = m_{\text{max}} = 0$. The simulation results are shown in Fig. 5, where Fig. 5(a)(b)(c) represent the evolution using the central difference scheme, while Fig. 5(d)(e)(f) represent the evolution using the TVD scheme. Values from yellow to red indicate positive values, while blue values indicate negative values. It can be observed that in the simulation of the central difference scheme, negative values appear in some positions, whereas the TVD scheme maintains the positivity of the distribution function.

4.2. Laser propagation in plasma with a linear density profile

To verify the TVD scheme and Maxwell equations of transverse fields, an incident laser propagating in a plasma with a constant density gradient is simulated. The simulation results are compared with the exact analytical solution [62], which is given by

$$E_{y0}(x') = 2\sqrt{\pi} \left(\frac{\omega_0 L}{c} \right)^{\frac{1}{6}} E_0 e^{i\phi} \text{Ai}(\eta), \quad (65)$$

where $\eta = (\omega_0^2/c^2 L)^{(1/3)}(x' - L)$, ω_0 , and E_0 are the frequency and amplitude of the incident laser, respectively, L is the length between the locations where the electron density is zero and the critical density, x' is the length between x and the location where the electron density is zero, and ϕ is a phase factor.

The distribution functions for both electrons and hydrogen ions are initialized to be Maxwellian with thermal velocities of 0.024 and 3.96×10^{-4} , respectively. The space coordinate x is in the range of 0 to 40. A plasma with a linear density profile is located in the range of 5 to 35, where the density increases from 0 to 7. An incident laser beam from the left boundary has an amplitude of 0.003 and a frequency of $\sqrt{5}$, i.e., the critical electron density is 5. The polarization is in the y direction. The maximum velocities of electrons and ions are 0.22 and 3.2×10^{-3} . The phase space is resolved with 256 x -cells, 96 v -cells for electrons and 72 v -cells for ions. For electrons, the maximum indices of harmonics are $l_{\text{max}} = m_{\text{max}} = 7$. The analytical solution assumes the ions are fixed. Therefore we set $l_{\text{max}} = m_{\text{max}} = 0$ for ions. The time step is $\Delta t = 0.02$, and the midpoint method is used as the temporal discretization method. The effect of collisions has been ignored.

The comparison of the transverse electric field E_y from the simulation and analytical results is shown in Fig. 6. The reason for selecting time $t = 139.46$ is that the standing wave has already been formed before this moment, and the oscillation reaches the maximum value at this moment. The two lines almost coincide, and the L_2 -norm of the difference between E_y and the exact analytical solution E_{y0} is calculated by

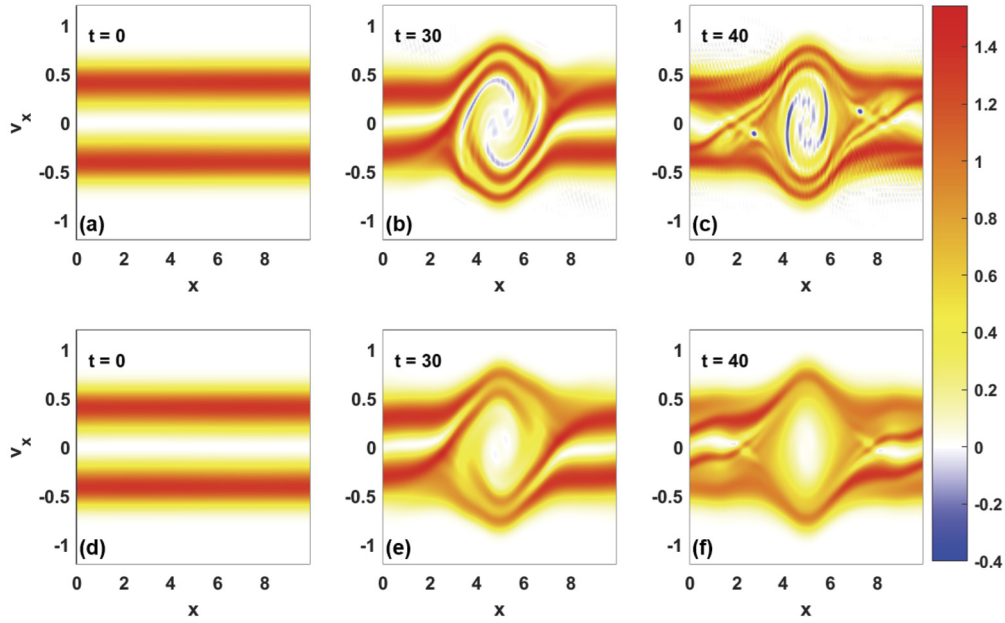


Fig. 5. Simulation results of the two-stream instability. The phase-space evolution of the electron distribution function is shown at the initial time, $\omega_{pe}t = 30$ and $\omega_{pe}t = 40$. Panels (a)(b)(c) depict the evolution using the central difference scheme, while panels (d)(e)(f) depict the evolution using the TVD scheme. All panels share the same colorbar: values greater than zero are represented from yellow to red, values less than zero are depicted in blue, and values around zero are represented in white.

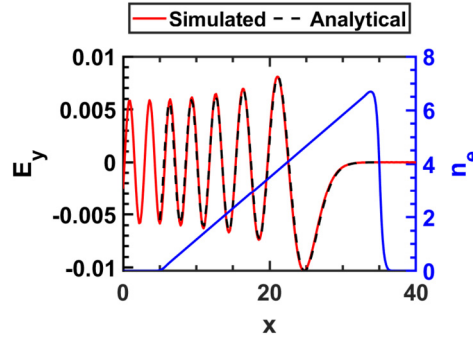


Fig. 6. Comparison of the transverse electric field E_y from the simulation and analytical results at $t = 139.46$. The red solid line represents the simulated amplitude of E_y , while the black dashed line represents the curve obtained by Eq. (65) in the range where the density is greater than zero. The phase factor ϕ is obtained by curve fitting and does not affect the shape and amplitude of the analytical curve. The blue solid line is drawn in the background corresponding to the electron density.

$$L_2 = \sqrt{\int (E_{y \text{ lx}} - E_{y0}(x_{\text{lx}}))^2 dx}, \quad (66)$$

which is 2.1×10^{-3} in this simulation result. Besides, there is no numerical instability in any region. And the simulation cannot be achieved if the central difference is applied for numerical instability.

4.3. Faraday rotation

The simulation of Faraday rotation [63] is a good example to examine the performance of the external static magnetic field when the distribution function is complex. It also embodies the ability of the code to simulate the three-dimensional velocity space.

The distribution function is initialized to be Maxwellian with thermal velocities of $0.024 c$ and $1.79 \times 10^{-4} c$. The density is homogeneous, with a length of $20 c/\omega_{pe}$. The two boundaries of the plasma are fixed to their initial values. The incident light is linearly polarized in the y -direction with an amplitude of $3 \times 10^{-4} m_e c \omega_{pe}/e$ and a frequency of $\sqrt{5} \omega_{pe}$. The phase space is resolved with 256 x -cells, 96 v -cells for electrons, and 48 v -cells for ions. We set $l_{\text{max}} = m_{\text{max}} = 7$ for electrons and $l_{\text{max}} = m_{\text{max}} = 0$ for ions. The time step is $\Delta t = 0.02 \omega_{pe}^{-1}$. The maximum velocities of electrons and ions are $0.16 c$ and $9.8 \times 10^{-4} c$. The phase angle $\phi = \arctan(E_z/E_y)$ has a relation of distance x [64]:

$$\phi = \frac{1}{2c} \left(\sqrt{\omega^2 - \frac{\omega_{pe}^2}{1 + \omega_{ce}/\omega}} - \sqrt{\omega^2 - \frac{\omega_{pe}^2}{1 - \omega_{ce}/\omega}} \right) x, \quad (67)$$

where $\omega_{ce} = eB_x/m_e$ is the electron cyclotron frequency, and B_x is the static magnetic field. It is shown that the phase angle ϕ has a linear relation with the distance x . From the simulation results, ϕ is obtained by calculating the envelope of E_z and E_y , and then taking

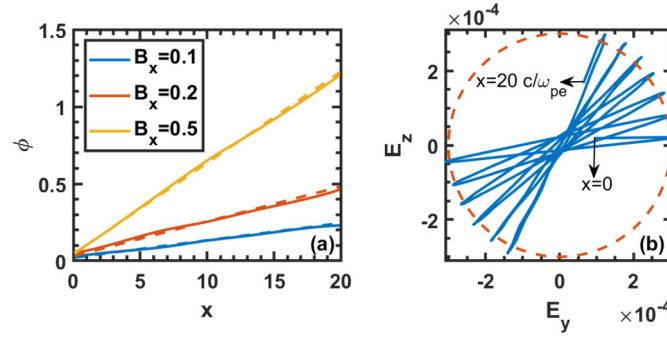


Fig. 7. (a) Comparison of the relation of the phase angle ϕ caused by Faraday rotation and x between the simulation results (solid lines) and the analytical results (dashed lines). (b) Variation of E_y and E_z with x in the polarization plane. The red dashed line represents a circle whose radius is the laser amplitude for comparison.

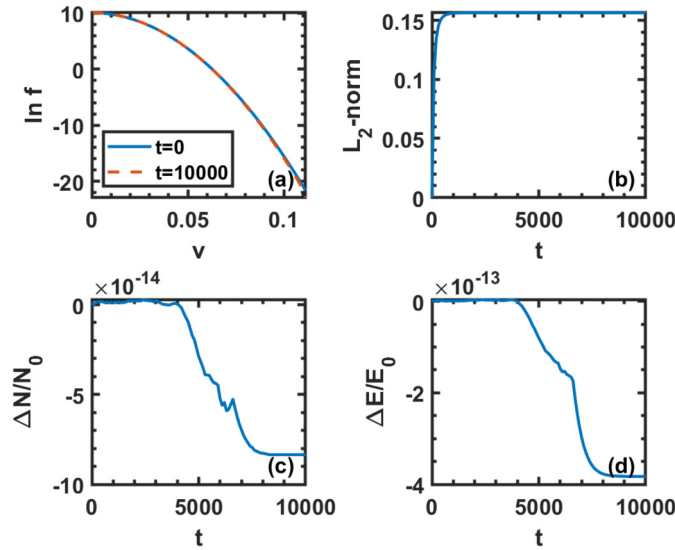


Fig. 8. Simulation results of the evolution of electrons whose initial density is already Maxwellian. (a) The logarithm of electron distribution function at $t=0$ and $t=10000 \omega_{pe}^{-1}$. (b) The L_2 -norm of the distribution function relative to the initial distribution. It remains nearly constant after $t=500 \omega_{pe}^{-1}$. (c) The relative change of total particle number versus time. (d) The relative change of total energy versus time.

the arctangent of their ratio. The relation between ϕ and x and their comparisons with Eq. (67) are shown in Fig. 7(a), where we can see they are in great agreement. The variation of E_y and E_z with x in the polarization plane is shown in Fig. 7(b). It can be seen that the amplitude remains relatively constant.

4.4. Static process

A simulation of a plasma that initially follows a Maxwellian distribution is conducted to observe whether it remains nearly unchanged over an extended period. This verification aims to demonstrate the effectiveness of the isotropic collision term and the modification approach.

The electron distribution function is initialized to be Maxwellian with a temperature of 100 eV. The velocity space of the electron is resolved with 108 cells. The maximum velocity in the velocity grid is 8.0 times the thermal velocity. The simulation is isotropic thus we set $l_{\max} = m_{\max} = 0$. The density of electrons is $8.928 \times 10^{21} \text{ cm}^{-3}$. Hence, the electron relaxation time $\tau_{ee} \approx 62 \omega_{pe}^{-1}$, and for hydrogen ions with a temperature of 10 eV, the ion relaxation time $\tau_{ii} \approx 472 \omega_{pe}^{-1}$. The total simulation time is $10000 \omega_{pe}^{-1}$ with the time step $\Delta t = 0.1$. The simulation results after conservation modification are shown in Fig. 8. From Fig. 8(a), it can be observed that even after more than 20 times the ion relaxation time, the distribution function, including its tail, has not changed significantly. The L_2 -norm of the difference between the simulated distribution f and the exact Maxwellian distribution f_0 is calculated by

$$L_2 = \sqrt{4\pi \int (f - f_0) v^2 dv}, \quad (68)$$

which is shown in Fig. 8(b). It can be seen that the distribution eventually becomes a stable state. From Fig. 8(c) and (d), it can be observed that particle number and energy are fully conserved.

For comparison, we conduct a simulation with all parameters identical to the previous one except without conservation modification. The simulation results are shown in Fig. 9. It can be seen that when conservation modification is not applied, the distribution function exhibits noticeable deviation over time. The deviations in particle number and energy also accumulate over time. Therefore, the discretized equations with conservation modification are highly effective.

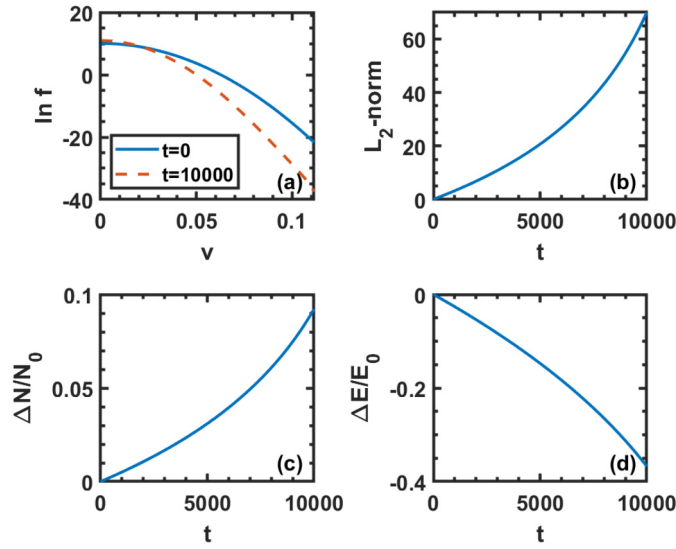


Fig. 9. Simulation results of the evolution of electrons whose initial density is already Maxwellian. Conservation modification is not applied in this simulation, while other simulation conditions and the caption are the same as those in Fig. 8. Compared to the simulation considering conservation modification, the results of this one are noticeably worse.

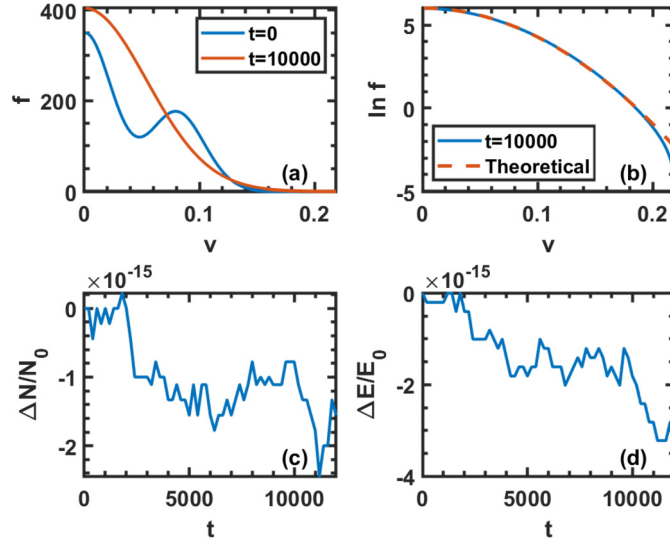


Fig. 10. Simulation of the non-Maxwellian electron relaxation process. (a) The electron distribution function at $t=0$ (blue solid line) and $t=10000 \omega_{pe}^{-1}$ (red solid line). (b) The logarithm of simulated distribution (blue solid line) and the logarithm of theoretical distribution (red dashed line). (c) The relative change of total particle number versus time. (d) The relative change of total energy versus time.

4.5. Isotropic relaxation of electrons

To further examine the conservation properties of collisions between the same species, we conduct a simulation with an unnormalized initial distribution

$$f(v)|_{t=0} = \frac{1}{v_{Te}^3} \exp\left(-\frac{v^2}{2v_{Te}^2}\right) + \frac{1}{2v_{Te}^3} \exp\left(-\frac{(v-v_d)^2}{2v_{Te}^2}\right), \quad (69)$$

where $v_{Te} = 0.024 c$ and $v_d = 0.08 c$. The velocity space of the electron is resolved with 96 cells. The maximum velocity in the velocity grid is $0.22 c$. The simulation is isotropic thus we set $l_{\max} = m_{\max} = 0$. The density of electrons is 10^{23} cm^{-3} . Hence, the electron relaxation time $\tau_{ee} \approx 717 \omega_{pe}^{-1}$. The time step is $\Delta t = 0.3$.

The simulation results after conservation modification are shown in Fig. 10. From Fig. 10(a), it can be observed that after about 14 times the electron relaxation time, the distribution function becomes Maxwellian. The comparison between the logarithm of simulated distribution and the logarithm of theoretical distribution is shown in Fig. 10(b), it can be seen that though it is not significant, the tail of the distribution function does not completely relax to Maxwellian. From Fig. 10(c) and (d), it can be observed that particle number and energy are fully conserved during the relaxation process.

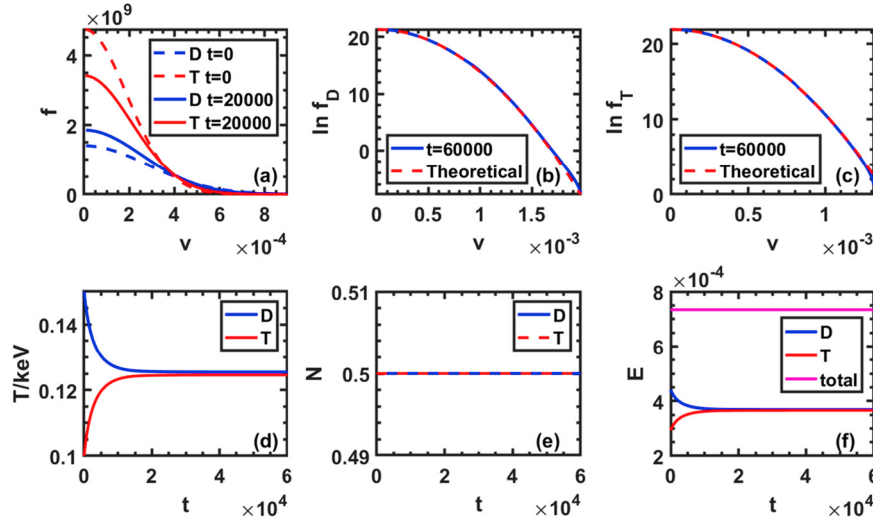


Fig. 11. Simulation results of the relaxation between D and T ions with different initial temperatures of 150 eV and 100 eV, respectively. (a) The distribution functions of D and T ions at $t = 0$ and $t = 20000 \omega_{pe}^{-1}$. (b) The temperatures of D and T ions versus time. They become equal over time. (c) The particle numbers of D and T ions versus time. (d) The energy of D, T ions, and the total energy versus time.

4.6. Relaxation between different ion species

To examine the performance for simulating the collisions between different ion species, we conduct a simulation of a DT plasma with the initial temperatures of both D and T ions Maxwellian. The initial temperatures of electrons, D ions, and T ions are 300 eV, 150 eV, and 100 eV, respectively. The ratio of particle numbers between D and T ions is 1 : 1. The number density of electrons is 10^{23} cm^{-3} . The typical relaxation times are $\tau_{DD} \approx 4.8 \times 10^3 \omega_{pe}^{-1}$ and $\tau_{TT} \approx 3.8 \times 10^3 \omega_{pe}^{-1}$.

The maximum velocities for the three velocity grids are seven times their respective thermal velocities, with grid sizes of 54, 108, and 108. The values of l_{\max} and m_{\max} for all species are zero. The time step $\Delta t = 0.2$.

The distribution functions at $t = 0$ and $t = 20000 \omega_{pe}^{-1}$ is shown in Fig. 11(a), where the temperature of D decreases and the temperature of T increases, indicating the occurrence of thermal conduction between D and T ions. The logarithm of D and T distributions at $t = 60000 \omega_{pe}^{-1}$ is shown in Fig. 11(b)(c), compared with the theoretical results. In this simulation, the tail of the distribution functions can relax to the Maxwellian distribution. The temperatures of these two ions are shown in Fig. 11(d). It can be seen that they become equal over time. The particle number and energy are shown in Fig. 11(f)(g), where the particle numbers of each species and the total energy are fully conserved.

4.7. Heat conduction

In order to verify the collision terms, we simulate the heat conduction and calculate the thermal conductivity κ in Fourier's law $\mathbf{q} = -\kappa \nabla T$. The simulation results are compared with the approximated analytical results in hydrodynamics limit [65]:

$$\kappa_e = \hat{\kappa}_e \frac{n_e T_e \tau_{ei}}{m_e}, \quad (70)$$

$$\kappa_i = \hat{\kappa}_i \frac{n_i T_i \tau_{ii}}{m_i}, \quad (71)$$

where the relaxation times are given by

$$\tau_{ei} = (4\pi\epsilon_0)^2 \frac{3m_e^{\frac{1}{2}} T_e^{\frac{3}{2}}}{4\sqrt{2\pi} n_e Z e^4 \ln \Lambda_{ei}}, \quad (72)$$

$$\tau_{ii} = (4\pi\epsilon_0)^2 \frac{3m_i^{\frac{1}{2}} T_i^{\frac{3}{2}}}{4\sqrt{\pi} n_i Z^2 e^4 \ln \Lambda_{ii}}. \quad (73)$$

The simulation results of thermal conductivity can be derived by $-q_x/(\partial T/\partial x)$, where the heat flux in x direction q_x from the simulation results are given by

$$q_x = m \left[2\pi V_x^2 \int_0^\infty f_1^0 v^3 dv - V_x \int_0^\infty \left(\frac{8\pi}{5} f_2^0 + \frac{7\pi}{3} f_0^0 \right) v^4 dv + \frac{2\pi}{3} \int_0^\infty f_1^0 v^5 dv \right], \quad (74)$$

where V_x is the macroscopic velocity in x direction

$$V_x = \frac{1}{n} \frac{4\pi}{3} \int_0^\infty f_1^0 v^3 dv. \quad (75)$$

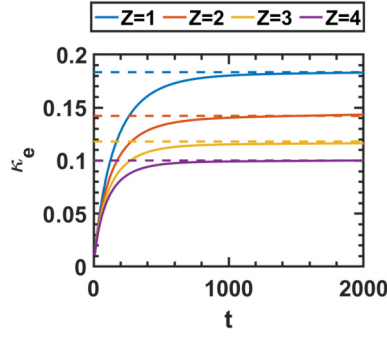


Fig. 12. Temporal evolution of simulated thermal conductivity of electron for $Z = 1, 2, 3, 4$ in the normalized units. The solid lines represent the simulated results obtained by $-q_x/(\partial T/\partial x)$, and the dashed lines represent the analytical results obtained by Eq. (70).

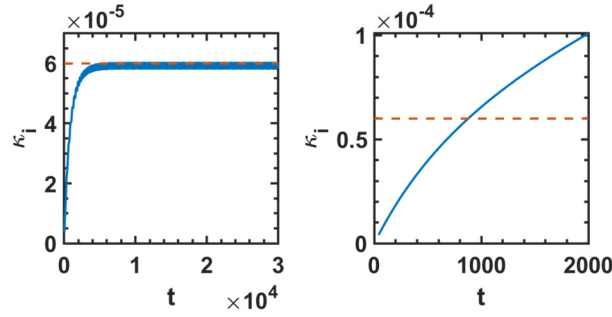


Fig. 13. Temporal evolution of thermal conductivity of ion in the normalized units. The blue solid lines represent the simulation results, while the red dashed lines represent the theoretical results obtained by Eq. (71). In the left panel, the motion of electrons is excluded by setting $l_{\max} = 0$ and $m_{\max} = 0$ for electrons, which demonstrates the accuracy of i - i collisions. In the right panel, the motion of electrons is included.

We first verify the electron thermal conductivity. The distribution function of electrons is initialized to be Maxwellian, and the temperature depends on x : $T_e(x) = 300 \text{ eV} + 6 \text{ eV} \times \sin(2\pi x/L)$. The density of electrons is homogeneous and is equal to $n_e = 10^{23} \text{ cm}^{-3}$. There is no need to resolve the mean free paths in the configuration space. The length of the configuration space is $10^4 c/\omega_{pe}$, much greater than the mean free paths of each particle with thermal velocities ($\sim 10^1 c/\omega_{pe}$), resolved by 108 grids. The boundary condition is periodic. Other parameters are set as follows: $N_v = 52$, $l_{\max} = 4$ and $m_{\max} = 0$ for both electrons and ions, the maximum value of velocities is 6 times their thermal velocities. The temporal evolution of simulated thermal conductivity for $Z = 1, 2, 3, 4$ and $m_i = 1, 4, 7, 9$ times proton mass is shown in Fig. 12. The time steps for the first three simulations are $\Delta t = 0.05 \omega_{pe}^{-1}$, while for the fourth simulation, it is $0.04 \omega_{pe}^{-1}$. It can be seen that the thermal conductivity tends to the theoretical value after several times τ_{ei} .

The next simulation is to simulate the ion thermal conductivity. We note that the derivation of Eq. (71) neglects the heat flux of electron. However, the heat flux of ions is much less than that of electrons. To demonstrate this feature and verify the ion-ion collisions, two simulations are performed though one of them is non-physical. In the first simulation, electrons are mobile, but in the second simulation, electrons are stationary. The distribution functions of ions are both initialized to be Maxwellian, and the temperatures are both $T_i(x) = 30 \text{ eV} + 0.6 \text{ eV} \times \sin(2\pi x/L)$. The electron temperature is 10 times the ion temperature and $Z = 1$. The time step is $0.1 \omega_{pe}^{-1}$. Other parameters are the same as the simulations of electron thermal conductivity. The simulation results are shown in Fig. 13. In the left panel, the motion of electrons is excluded by setting $l_{\max} = m_{\max} = 0$ for electrons, only the motion of ions is considered. The simulated ion thermal conductivity is in good agreement with Eq. (71) and oscillates with ion plasma frequency ω_{pi} . In the right panel, it is shown that the motion of electrons significantly affects ion heat conduction.

4.8. Inverse bremsstrahlung absorption

We simulate the absorption of the laser energy mainly caused by electron-ion collisions, as an example of a combination of both laser propagation and collisions. For a linear density profile, the energy absorption rate can be theoretically calculated by using WKB approximation [62]

$$\alpha = 1 - \exp\left(-\frac{32\nu_{ei}^* L}{15c}\right), \quad (76)$$

where ν_{ei}^* is the collision frequency at the critical density, and L is the length from $n_e = 0$ to n_{cr} . In the simulation, this value can be obtained by dividing the energy flux averaged over several periods on the incident boundary $\langle E_y B_z \rangle$, by the averaged energy flux of the incident laser $E_y^2/2c$. We set $L = 6 \mu\text{m}$, laser wavelength $\lambda_L = 0.524 \mu\text{m}$, and laser amplitude $E_y = 10^{-5} m_e c \omega_L/e$ to avoid the apparent increase of electron temperature, where ω_L is the laser frequency.

The collision frequency is changed by adjusting electron temperatures in the range $T_e = 1.0, 1.5, 2.0, 2.5, 3.0, 3.5, 4.0, 5.0, 5.5 \text{ keV}$ and their corresponding $Z = 41, 43, 45, 47, 49, 51, 48, 46, 36$. High- Z plasmas are selected to neglect the influence of e - e collisions. The time step is $0.02 \omega_L^{-1}$. The configuration space is resolved with 256 x -cells. For the first five simulations, the length of the vacuum on the left side of the plasma is $5 c/\omega_L$, and the total simulation length is $90 c/\omega_L$. We set $l_{\max} = 6$ and $m_{\max} = 3$ for electrons, and $l_{\max} = m_{\max} = 0$ for ions. The maximum value of the electron velocity grid is 5.5 times the thermal velocity, resolved by 44 grids. For the last four

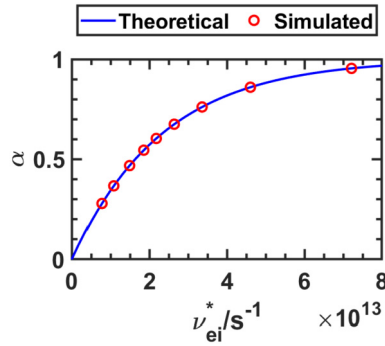


Fig. 14. Comparison of the theoretical absorption rate obtained by Eq. (76) with the simulation results. The blue dashed line represents the theoretical results obtained by Eq. (76), while the red circles represent the results of simulations with different Z and T_e .

simulations, collisions become weak and more harmonics are required. Therefore the values of l_{\max} and m_{\max} are changed to 12 and 4, respectively. The length of the vacuum on the left side of the plasma is changed to $15 c/\omega_L$, and the total simulation length is changed to $90 c/\omega_L$. The maximum value of the electron velocity grid is changed to 6.5 times the thermal velocity, resolved by 52 grids.

The energy flux is calculated by averaging the four periods before $t = 440 \omega_{pe}^{-1}$, when the reflected light has already returned to the incident boundary, and the standing wave has formed. The simulation results are shown in Fig. 14. It is shown that the simulation of inverse bremsstrahlung absorption is in great agreement with Eq. (76) and better than the results of PIC simulations [66].

4.9. Return current instability

Temperature gradient leads to the transport of a population of hot electrons, then another population of cold electrons is accelerated by the electrostatic field in the opposite direction. This convection can drive an instability of ion acoustic wave (IAW). This process is known as return current instability (RCI). RCI involves electron thermal transport and excitation of IAW. Therefore it is affected by all kinds of collisions. Though RCI can be theoretically studied by Spitzer-Härm transport theory, it is only valid in strong $e-i$ collision situations and small temperature gradient of electrons. Under this condition, the growth rate may be less than the damping rate of IAW, and RCI does not occur. The non-local effects have been studied in Ref. [67], and a theoretical expression is given in the range of $0 < k\lambda_{ei} < 100$. By neglecting the dependence of collisions on the frequency of IAW and ignoring the damping of IAW, theoretical analysis reveals that under typical non-local transport conditions, the wave number with maximum growth rate k_{\max} is approximately smaller than $0.7/\lambda_{De}$. Moreover, when ion collisions are taken into account, both the growth rate and k_{\max} are reduced compared to the case without ion collisions.

We simulate this instability to see the performance in the non-local regime of electron thermal transport. The initial density of electrons $n_e = 1.0 \times 10^{20} \text{ cm}^{-3}$ is homogeneous, with a temperature profile $T_e(x)|_{t=0} = 1 \text{ keV} + 0.6 \text{ keV} \times \exp(-(x-50)^2/8.33^2)$, respectively. The boundary condition is periodic. The initial density and temperature of ions are both homogeneous with $T_e/T_i = 40$ and $Z = 1$. The mass of ions is set to $100m_e$ to save calculation time. The total simulation length is $100 c/\omega_{pe}$ with 5000 x-cells and 66 v-cells for both electrons and ions. We set $l_{\max} = 3$ and $m_{\max} = 0$ for both electrons and ions. The time step is $5 \times 10^{-3} \omega_{pe}^{-1}$. To maintain the temperature gradient, we add a phenomenological heat source by substitute the isotropic electron distribution function f_0^0 with $\alpha f_{\text{hot}}(x) + (1-\alpha)f_0^0$ in each time step, where $\alpha = 10^{-3}$ and $f_{\text{hot}}(x)$ is Maxwellian with a temperature of $T_{e \text{ hot}}(x) = T_e(x)|_{t=0}$. Fig. 15 illustrates the simulation results without ion collisions and with ion collisions, where RCI occurs at around $t = 600 \omega_{pe}^{-1}$ and $t = 500 \omega_{pe}^{-1}$, respectively. Fig. 15(a) displays a pseudocolor plot of the relationship between E_k , wavenumber, and time. The upper plot corresponds to the case without ion collisions, while the lower plot includes ion collisions. Fig. 15(b) displays the growth of E_k , which has been averaged within the range of $k\lambda_{De} = 0.15$ to $k\lambda_{De} = 0.8$. It can be observed that the growth rate without ion collisions is greater than that with ion collisions, and the growth without ion collisions is later than that with ion collisions. Fig. 15(c) displays E_k versus $k\lambda_{De}$ at time $t = 688 \omega_{pe}^{-1}$ and $t = 665 \omega_{pe}^{-1}$. It can be seen that the k_{\max} without ion collisions is greater than that with ion collisions, and the wavenumber spectrum with ion collisions is more concentrated than that without ion collisions.

5. Discussion and conclusion

A 1D3V Vlasov-Fokker-Planck-Maxwell code is developed, which contains multiple ion species, collisions involving all kinds of particles, relativistic electrons, and external lasers. All species are treated by kinetic distribution functions, which can possess independent velocity (momentum) grids and harmonics. The particle numbers for each particle, the individual energies for collisions between the same species, and the total energy for collisions between different species are all conserved. The TVD scheme is also applied to inhibit numerical instability that occurs in the region of steep density, rarefied plasma-vacuum interface, and non-periodic boundary conditions. The correctness of the code has been verified by several simulation results given in this paper.

The phase space discretization methods employed by the code consist of second-order difference, trapezoidal integration, and linear interpolation. The temporal discretization employs the Runge-Kutta method, typically choosing a second-order scheme (the midpoint method), resulting in an order of accuracy of $O(\Delta x^2) + \sum_{\beta} O(\Delta v_{\beta}^2) + O(\Delta t^2)$.

The code is fully explicit. The determination of the value of the time step Δt should be small enough to resolve the electron oscillation and electromagnetic oscillation. However, the Vlasov-Fokker-Planck-Maxwell equations are non-linear. Thus the exact value of Δt is hard to decide and may change over time. To this end, the code is designed to be interrupted automatically once the numerical instability is detected. Then the user can reduce the time step and continue computing from the files saved at the breakpoint.

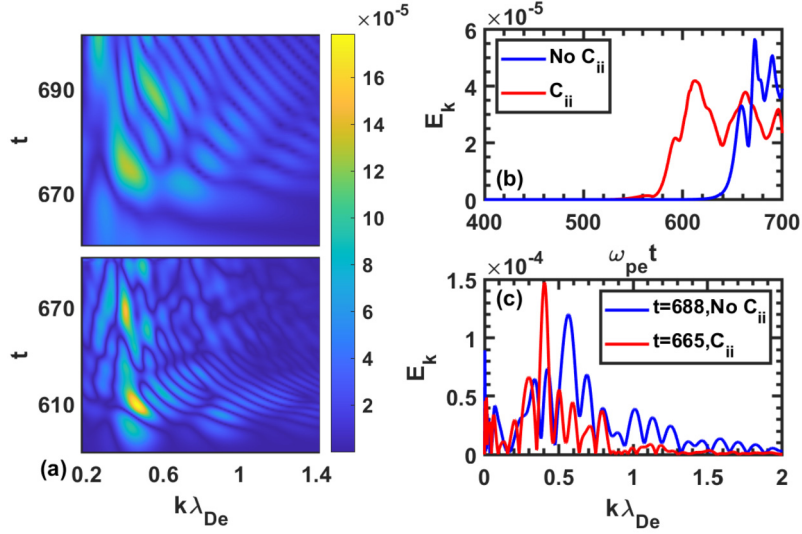


Fig. 15. The simulation results of RCI. (a) Pseudocolor plot of the relationship between E_k , $k\lambda_{De}$, and t . The upper plot corresponds to the case without ion collisions, while the lower plot includes ion collisions. (b) E_k averaged within the range of $k\lambda_{De} = 0.15$ to $k\lambda_{De} = 0.8$. (c) E_k versus $k\lambda_{De}$ at time $t = 688 \omega_{pe}^{-1}$ without ion collisions and $t = 665 \omega_{pe}^{-1}$ with ion collisions.

The discretized equations are expressed as the product of multidimensional arrays, enabling the utilization of well-established matrix multiplication algorithms for efficient calculations. This approach allows for the possibility of achieving high-performance parallel computations on large-scale systems in the future.

The code also has some limitations. Firstly, in the calculation of electron-ion collisions, ions are assumed to be immobile. Despite the modification of considering the ion drift velocity in Ref. [45], the isotropic part $\partial f_0^0 / \partial t$ remains zero, implying that electron-ion collisions cannot lead to energy exchange. If the simulation involves ion-electron collisions, the total energy is not conserved. This problem cannot be solved easily, as the dominant part of the isotropic electron-ion collision integral is much smaller compared to the first velocity grid of electrons. Secondly, the program employs a “semi-anisotropic approximation”, making it unsuitable for simulating extreme drift situations where f_1^m is greater than f_0^0 or comparable to it. The momentum in the physical model is also not conserved. Thirdly, grids of phase space are uniform, which is not suitable for simulating cases with locally higher resolution.

Declaration of competing interest

The authors declare that they have no known competing financial interests or personal relationships that could have appeared to influence the work reported in this paper.

Data availability

Data will be made available on request.

Acknowledgements

This work is supported by the National Natural Science Foundation of China (Grant Nos. 11975059, 12005021, 11875091, and 11875241).

Appendix A. Multidimensional arrays

While the code can achieve better results with the TVD scheme, here we provide the multidimensional array elements for the central difference scheme. This is because in the discretized equation (42) of the TVD scheme, the first term corresponds to the central difference. The multidimensional array elements of the advection term are given by

$$\mathcal{A}_{lx, l, lm}^{lx0, l, lm0} = -\frac{1}{2\Delta x} (\delta_{lx+1}^{lx0} - \delta_{lx-1}^{lx0}) \left[\frac{l-m}{2l-1} \delta_{l(l-1)m}^{l, lm0} + \frac{l+m+1}{2l+3} \delta_{l(l+1)m}^{l, lm0} \right], \quad (77)$$

where the symbol δ is defined as

$$\delta_l^{l0} = \begin{cases} 0, & l \neq l0 \\ 1, & l = l0 \end{cases}. \quad (78)$$

When applying the TVD scheme, the multidimensional array elements of the advection term are first modified to become

$$\tilde{\mathcal{A}}_{lx, l, lm}^{lx0, l, lm0} = \mathcal{A}_{lx, l, lm}^{lx0, l, lm0} + L_k^{l, lm0} |a_k| R_{lm}^k (\delta_{lx+1}^{lx0} - 2\delta_{lx}^{lx0} + \delta_{lx-1}^{lx0}), \quad (79)$$

where the definitions of L_k^{llm0} , a_k and R_{llm}^k have been provided in the main text. The elements of $\overline{\mathcal{H}}$ in the TVD scheme are given by

$$\overline{\mathcal{H}}_{lx,lv,k} = |a_k| L_k^{llm0} (\delta_{lx-1}^{lx0} - \delta_{lx-2}^{lx0}), \quad (80)$$

note that lx ranges from 1 to $N_x + 3$.

The multidimensional arrays, which are not related to collisions between different ion species, involve the velocity mesh of only one species. Thus, we omit the subscript of species α temporarily. The elements of the multidimensional array of longitudinal electric field for $lv > 1$ if $llm > 1$, or $lv > lvc$ if $llm = 1$ are given by

$$\mathcal{E}_{x,lv,llm}^{lv0,llm0} = -\frac{Z_\alpha}{M_\alpha} \left[\frac{l-m}{2l-1} \left(\frac{v_{lv}}{v_{lv0}} \right)^{l-1} \delta_{l(l-1)m}^{llm0} \mathcal{D}_{lv}^{lv0} + \frac{l+m+1}{2l+3} \left(\frac{v_{lv}}{v_{lv0}} \right)^{-l-2} \delta_{l(l+1)m}^{llm0} \mathcal{D}_{lv}^{lv0} \right], \quad (81)$$

where \mathcal{D}_{lv}^{lv0} represents a matrix of the first derivative of v , for the case of a uniform mesh, it is defined as

$$\mathcal{D}_{lv}^{lv0} = \frac{1}{2\Delta v} (\delta_{lv+1}^{lv0} - \delta_{lv-1}^{lv0}). \quad (82)$$

For $lv \leq lvc$ and $llm = 1$, the elements are

$$\mathcal{E}_{x,lv \leq lvc,llm=1}^{lv0,llm0} = -\frac{Z_\alpha}{3M_\alpha} \left(3D_A^{lv0} + 4D_B^{lv0} v_{lv} + 5D_C^{lv0} v_{lv}^2 + 6D_D^{lv0} v_{lv}^3 \right) \delta_{l10}^{llm0}, \quad (83)$$

where

$$\begin{aligned} D_A^{lv0} &= \frac{1}{D} \begin{vmatrix} \delta_1^{lv0} & v_1^2 & v_1^3 & v_1^4 \\ \delta_2^{lv0} & v_2^2 & v_2^3 & v_2^4 \\ \delta_3^{lv0} & v_3^2 & v_3^3 & v_3^4 \\ \delta_4^{lv0} & v_4^2 & v_4^3 & v_4^4 \end{vmatrix}, D_B^{lv0} = \frac{1}{D} \begin{vmatrix} v_1 & \delta_1^{lv0} & v_1^3 & v_1^4 \\ v_2 & \delta_2^{lv0} & v_2^3 & v_2^4 \\ v_3 & \delta_3^{lv0} & v_3^3 & v_3^4 \\ v_4 & \delta_4^{lv0} & v_4^3 & v_4^4 \end{vmatrix}, \\ D_C^{lv0} &= \frac{1}{D} \begin{vmatrix} v_1 & v_1^2 & \delta_1^{lv0} & v_1^4 \\ v_2 & v_2^2 & \delta_2^{lv0} & v_2^4 \\ v_3 & v_3^2 & \delta_3^{lv0} & v_3^4 \\ v_4 & v_4^2 & \delta_4^{lv0} & v_4^4 \end{vmatrix}, D_D^{lv0} = \frac{1}{D} \begin{vmatrix} v_1 & v_1^2 & v_1^3 & \delta_1^{lv0} \\ v_2 & v_2^2 & v_2^3 & \delta_2^{lv0} \\ v_3 & v_3^2 & v_3^3 & \delta_3^{lv0} \\ v_4 & v_4^2 & v_4^3 & \delta_4^{lv0} \end{vmatrix}, \end{aligned} \quad (84)$$

and

$$D = \begin{vmatrix} v_1 & v_1^2 & v_1^3 & v_1^4 \\ v_2 & v_2^2 & v_2^3 & v_2^4 \\ v_3 & v_3^2 & v_3^3 & v_3^4 \\ v_4 & v_4^2 & v_4^3 & v_4^4 \end{vmatrix}. \quad (85)$$

Note that these determinants are only applicable to terms related to the electric field.

For $lv = 1$ and $llm > 1$, we have [58]

$$\mathcal{E}_{x,lv=1,llm>1}^{lv0,llm0} = -\frac{Z_\alpha}{M_\alpha} \left[\frac{l-m}{2l-1} K_1 \delta_{llm}^{l10} \delta_{l00}^{llm0} (\delta_2^{lv0} - \delta_1^{lv0}) + \frac{l+m+1}{2l+3} K_2 \delta_{l(l+1)m}^{llm0} \delta_2^{lv0} \right], \quad (86)$$

where K_1 and K_2 are defined as

$$K_1 = \frac{1}{v_2 - v_1} \frac{1}{1 + \frac{v_2 - v_1}{2v_1}}, \quad K_2 = (2l+3) \frac{(v_1)^l}{(v_2)^{l+1}}. \quad (87)$$

When $lv > 1$ if $llm > 1$, or $lv > lvc$ if $llm = 1$, the elements of multidimensional arrays of the transverse electric field are given by

$$\mathcal{E}_{yz,lv,ll(m=0)}^{lv0,llm0} = -\frac{Z_\alpha}{M_\alpha} \left[-\frac{l(l-1)}{2l-1} \left(\frac{v_{lv}}{v_{lv0}} \right)^{l-1} \delta_{l(l-1)1}^{llm0} \mathcal{D}_{lv}^{lv0} + \frac{(l+1)(l+2)}{2l+3} \left(\frac{v_{lv}}{v_{lv0}} \right)^{-l-2} \delta_{l(l+1)1}^{llm0} \mathcal{D}_{lv}^{lv0} \right]. \quad (88)$$

For $lv \leq lvc$ and $llm = 1$, we have

$$\mathcal{E}_{yz,lv \leq lvc,l00}^{lv0,llm0} = -\frac{2Z_\alpha}{3M_\alpha} \left(3D_A^{lv0} + 4D_B^{lv0} v_{lv} + 5D_C^{lv0} v_{lv}^2 + 6D_D^{lv0} v_{lv}^3 \right) \delta_{l11}^{llm0}. \quad (89)$$

For $lv = 1$ and $llm > 1$, we have

$$\mathcal{E}_{yz,lv=1,l(l>0)(m=0)}^{lv0,llm0} = -\frac{Z_\alpha}{M_\alpha} \frac{(l+1)(l+2)}{2l+3} K_2 \delta_{l(l+1)m}^{llm0} \delta_2^{lv0}. \quad (90)$$

The elements of other multidimensional arrays of the transverse electric field with $m > 0$ are given by

$$\mathcal{E}_{yz,lv>1,ll(m>0)}^{lv0,llm0} = -\frac{Z_\alpha}{2M_\alpha} \left[\frac{1}{2l-1} \left(\frac{v_{lv}}{v_{lv0}} \right)^{l-1} \delta_{l(l-1)(m-1)}^{llm0} \mathcal{D}_{lv}^{lv0} - \frac{1}{2l+3} \left(\frac{v_{lv}}{v_{lv0}} \right)^{-l-2} \delta_{l(l+1)(m-1)}^{llm0} \mathcal{D}_{lv}^{lv0} \right], \quad (91)$$

$$\mathcal{E}_{yz-}^{lv0, llm0}_{lv=1, ll(m>0)} = -\frac{Z_\alpha}{2M_\alpha} \left[\frac{1}{2l-1} K_1 \delta_{llm}^{l11} \delta_{l00}^{llm0} - \frac{1}{2l+3} K_2 \delta_{l(l+1)(m-1)}^{llm0} \delta_2^{lv0} \right], \quad (92)$$

$$\begin{aligned} \mathcal{E}_{yz+}^{lv0, llm0}_{lv>1, ll(m>0)} = & -\frac{Z_\alpha}{2M_\alpha} \left[-\frac{(l-m)(l-m-1)}{2l-1} \left(\frac{v_{lv}}{v_{lv0}} \right)^{l-1} \delta_{l(l-1)(m+1)}^{llm0} \mathcal{D}_{lv}^{lv0} \right. \\ & \left. + \frac{(l+m+1)(l+m+2)}{2l+3} \left(\frac{v_{lv}}{v_{lv0}} \right)^{-l-2} \delta_{l(l+1)(m+1)}^{llm0} \mathcal{D}_{lv}^{lv0} \right], \end{aligned} \quad (93)$$

$$\mathcal{E}_{yz+}^{lv0, llm0}_{lv=1, ll(m>0)} = -\frac{Z_\alpha}{2M_\alpha} \frac{(l+m+1)(l+m+2)}{2l+3} K_2 \delta_{l(l+1)(m+1)}^{llm0} \delta_2^{lv0}. \quad (94)$$

The elements of multidimensional arrays of the magnetic field are given by

$$\mathcal{B}_{x \ llm} = \frac{imZ_\alpha}{M_\alpha}, \quad (95)$$

$$\mathcal{B}_{yz0}^{llm0}_{ll(m=0)} = -\frac{Z_\alpha}{M_\alpha} l(l+1) \delta_{ll1}^{llm0}, \quad (96)$$

$$\mathcal{B}_{yz+}^{llm0}_{ll(m>0)} = \frac{Z_\alpha}{2M_\alpha} \delta_{ll(m-1)}^{llm0}, \quad (97)$$

$$\mathcal{B}_{yz-}^{llm0}_{ll(m>0)} = -\frac{Z_\alpha}{2M_\alpha} (l-m)(l+m+1) \delta_{ll(m+1)}^{llm0}. \quad (98)$$

For isotropic part of collision terms, we first define three two-dimensional arrays I_1^{lv2} , I_2^{lv2} and I_3^{lv2} corresponding to three integrals $\int_v^\infty F(u)u du$, $\int_0^v F(u)u^2 du$ and $\int_0^v F(u)u^4 du$ in Eq. (18), respectively. The definition of the asterisk is the same as that in the main text. Their elements are given by

$$\begin{aligned} I_1^{lv2} = & \frac{1}{2} v_{lv2}^* \Delta v^* \begin{cases} 1, lv2 = lvp \\ 2, lv2 > lvp \\ 0, lv2 < lvp \end{cases} + \frac{1}{2} v_{lv2}^* (v_{lvp}^* - v_{lv}) \\ & \times \left[\begin{cases} \frac{1}{\Delta v^*} \left[(v_{lvp}^* - v_{lv}) \delta_{lvp-1}^{lv2} + (v_{lv} - v_{lvp-1}^*) \delta_{lvp}^{lv2} \right], & v_{lv} > v_1^* \\ \frac{v_{lv}}{v_1^*} \delta_1^{lv2}, & v_{lv} \leq v_1^* \end{cases} + \delta_{lvp}^{lv2} \right]. \end{aligned} \quad (99)$$

For $lv2 \leq lvc^*$,

$$I_2^{lv2 \leq lvc} = \frac{1}{3} D_0^{*lv2} v_{lv}^3 + \frac{1}{5} D_A^{*lv2} v_{lv}^5 + \frac{1}{6} D_B^{*lv2} v_{lv}^6 + \frac{1}{7} D_C^{*lv2} v_{lv}^7, \quad (100)$$

$$I_3^{lv2 \leq lvc} = \frac{1}{5} D_0^{*lv2} v_{lv}^5 + \frac{1}{7} D_A^{*lv2} v_{lv}^7 + \frac{1}{8} D_B^{*lv2} v_{lv}^8 + \frac{1}{9} D_C^{*lv2} v_{lv}^9, \quad (101)$$

where

$$\begin{aligned} D_0^{*lv2} = & \frac{1}{D} \begin{vmatrix} \delta_1^{lv2} & v_1^{*2} & v_1^{*3} & v_1^{*4} \\ \delta_2^{lv2} & v_2^{*2} & v_2^{*3} & v_2^{*4} \\ \delta_3^{lv2} & v_3^{*2} & v_3^{*3} & v_3^{*4} \\ \delta_4^{lv2} & v_4^{*2} & v_4^{*3} & v_4^{*4} \end{vmatrix}, D_A^{*lv2} = \frac{1}{D} \begin{vmatrix} 1 & \delta_1^{lv2} & v_1^{*3} & v_1^{*4} \\ 1 & \delta_2^{lv2} & v_2^{*3} & v_2^{*4} \\ 1 & \delta_3^{lv2} & v_3^{*3} & v_3^{*4} \\ 1 & \delta_4^{lv2} & v_4^{*3} & v_4^{*4} \end{vmatrix}, \\ D_B^{*lv2} = & \frac{1}{D} \begin{vmatrix} 1 & v_1^{*2} & \delta_1^{lv2} & v_1^{*4} \\ 1 & v_2^{*2} & \delta_2^{lv2} & v_2^{*4} \\ 1 & v_3^{*2} & \delta_3^{lv2} & v_3^{*4} \\ 1 & v_4^{*2} & \delta_4^{lv2} & v_4^{*4} \end{vmatrix}, D_C^{*lv2} = \frac{1}{D} \begin{vmatrix} 1 & v_1^{*2} & v_1^{*3} & \delta_1^{lv2} \\ 1 & v_2^{*2} & v_2^{*3} & \delta_2^{lv2} \\ 1 & v_3^{*2} & v_3^{*3} & \delta_3^{lv2} \\ 1 & v_4^{*2} & v_4^{*3} & \delta_4^{lv2} \end{vmatrix}, \end{aligned} \quad (102)$$

and

$$D = \begin{vmatrix} 1 & v_1^{*2} & v_1^{*3} & v_1^{*4} \\ 1 & v_2^{*2} & v_2^{*3} & v_2^{*4} \\ 1 & v_3^{*2} & v_3^{*3} & v_3^{*4} \\ 1 & v_4^{*2} & v_4^{*3} & v_4^{*4} \end{vmatrix}. \quad (103)$$

For $lv2 > lvc^*$,

$$I_{2lv}^{lv2>lv c} = \frac{1}{2} v_{lv2}^{*2} \Delta v^* \begin{cases} 1, lv2 = 1 \text{ or } lvm \\ 2, 1 < lv2 < lvm \\ 0, lv2 > lvm \end{cases} + \frac{1}{2} v_{lv2}^{*2} v_1^* \delta_1^{lv2} \\ + \begin{cases} \frac{v_{lv2}^{*2} (v_{lv} - v_{lvm}^*)}{2} \left[\frac{(v_{lvm+1}^* - v_{lv}) \delta_{lvm}^{lv2} + (v_{lv} - v_{lvm}^*) \delta_{lvm+1}^{lv2}}{\Delta v^*} + \delta_{lvm}^{lv2} \right], & v_{lv} < v_{Nv}^* \\ 0, & v_{lv} \geq v_{Nv}^* \end{cases}, \quad (104)$$

$$I_{3lv}^{lv2>lv c} = \frac{1}{2} v_{lv2}^{*4} \Delta v^* \begin{cases} 1, lv2 = 1 \text{ or } lvm \\ 2, 1 < lv2 < lvm \\ 0, lv2 > lvm \end{cases} + \frac{1}{2} v_{lv2}^{*4} v_1^* \delta_1^{lv2} \\ + \begin{cases} \frac{v_{lv2}^{*4} (v_{lv} - v_{lvm}^*)}{2} \left[\frac{(v_{lvm+1}^* - v_{lv}) \delta_{lvm}^{lv2} + (v_{lv} - v_{lvm}^*) \delta_{lvm+1}^{lv2}}{\Delta v^*} + \delta_{lvm}^{lv2} \right], & v_{lv} < v_{Nv}^* \\ 0, & v_{lv} \geq v_{Nv}^* \end{cases}. \quad (105)$$

Then we define another two-dimensional array δ^{*lv2} corresponding to the value of F expressed on the grid of f , which is given by

$$\delta^{*lv2} = \begin{cases} \frac{1}{\Delta v^*} \left[(v_{lvm}^* - v_{lv}) \delta_{lvm}^{lv2} + (v_{lv} - v_{lvm}^*) \delta_{lvm+1}^{lv2} \right], & lvm > lvc^* \text{ and } v_{lv} < v_{Nv}^* \\ D_0^{lv2} + D_A^{lv2} v_{lv}^2 + D_B^{lv2} v_{lv}^3 + D_C^{lv2} v_{lv}^4, & lvm \leq lvc \text{ or } lvm \text{ does not exist} \\ 0, & v_{lv} \geq v_{Nv}^* \end{cases} \quad (106)$$

Next, we define two two-dimensional arrays corresponding to the first and second derivatives of f . For $lv \leq lvc$, they are given by

$$\partial \delta_{lv}^{lv1} = 2D_A^{lv1} v_{lv} + 3D_B^{lv1} v_{lv}^2 + 4D_C^{lv1} v_{lv}^3, \quad (107)$$

$$\partial^2 \delta_{lv}^{lv1} = 2D_A^{lv1} + 6D_B^{lv1} v_{lv} + 12D_C^{lv1} v_{lv}^2, \quad (108)$$

where the definitions of D_A , D_B , and D_C are analogous to the definitions of D_A^* , D_B^* , and D_C^* in Eqs. (102) and (103) by removing all asterisks. For $lv > lvc$, they are given by

$$\partial \delta_{lv}^{lv1} = \frac{\delta_{lv+1}^{lv1} - \delta_{lv-1}^{lv1}}{2\Delta v}, \quad (109)$$

$$\partial^2 \delta_{lv}^{lv1} = \frac{\delta_{lv+1}^{lv1} - 2\delta_{lv}^{lv1} + \delta_{lv-1}^{lv1}}{\Delta v^2}. \quad (110)$$

Finally, the elements of multidimensional arrays of the isotropic part of collision terms are given by

$$\mathcal{C}_{iso, \alpha\beta}^{lv1, lv2} = \frac{4\pi}{3} \left[\frac{3}{\mu} \delta_{lv}^{lv1} \delta^{*lv2} + \partial \delta_{lv}^{lv1} \left(\frac{3}{\mu} \frac{1}{v_{lv}^2} I_{2lv}^{lv2} - \frac{1}{v_{lv}^4} I_{3lv}^{lv2} + \frac{2}{v_{lv}} I_{1lv}^{lv2} \right) \right. \\ \left. + \partial^2 \delta_{lv}^{lv1} \left(\frac{1}{v_{lv}^3} I_{3lv}^{lv2} + I_{1lv}^{lv2} \right) \right]. \quad (111)$$

For the e - i collisions of ion species α , the collision term can be especially simplified as

$$(C_{e\alpha})_l^m = -\frac{l(l+1)}{2} \frac{\Gamma_{e\alpha}}{v^3} (f_e)_l^m \times 4\pi \int_0^\infty v^2 (f_\alpha)_0^0 dv \quad (112)$$

and discretized as

$$(C_{e\alpha})_{lx, lv, lvm} = C_{e\alpha}^{lv0}{}_{lv, lvm} (f_\alpha)_{lx, lv0, 100} (f_e)_{lx, lv, lvm}. \quad (113)$$

The multidimensional array $C_{e\alpha}$ is given by [68,69]

$$C_{e\alpha}^{lv0}{}_{lv, lvm} = -2\pi l(l+1) \Gamma_{e\alpha} v_{lv} (v_\alpha)_{lv0}^2 g_{1, Nv\alpha}^{lv0}, \quad (114)$$

where v_{lv} is the velocity-dependent electron-ion collision frequency [69]

$$v_{lv} = \begin{cases} \frac{100}{v_{th}^3}, & v_{lv} \leq 100^{-\frac{1}{3}} v_{th} \\ \frac{1}{(v_e)_{lv}^3}, & 100^{-\frac{1}{3}} v_{th} < v_{lv} \leq 6v_{th} \\ \frac{1}{(v_e)_{lv}^3} \left[1 - \sin^2 \left(\frac{\pi}{2} \frac{v - 6v_{th}}{v_{th}} \right) \right], & 6v_{th} < v_{lv} \leq 7v_{th} \\ 0, & v > 7v_{th} \end{cases}, \quad (115)$$

and v_{th} is the approximate thermal velocity of electrons. In the simulations, the values of v_{th} and other coefficients in Eq. (115) have little effect on the results.

To provide the elements of the multidimensional array $\mathcal{C}_{\text{Ani},00}^{lv1,lv2}_{lv,l(l \geq 1)m}$, we define

$$I_{1lv}^{lv2} = \frac{1}{2} v_{lv2}^{*l+2} \Delta v^* \begin{cases} 1, lv2 = 1 \text{ or } lvm \\ 2, 1 < lv2 < lvm \\ 0, lv2 > lvm \end{cases} + \frac{1}{2} v_{lv2}^{*l+2} v_1^* \delta_1^{lv2} \\ + \begin{cases} \frac{v_{lv2}^{*l+2} (v_{lv} - v_{lvm}^*)}{2} \left[\frac{(v_{lvm+1}^* - v_{lv}) \delta_{lvm}^{lv2} + (v_{lv} - v_{lvm}^*) \delta_{lvm+1}^{lv2}}{\Delta v^*} + \delta_{lvm}^{lv2} \right], & v_{lv} < v_{Nv}^* \\ 0, & v_{lv} \geq v_{Nv}^* \end{cases}, \quad (116)$$

$$I_{2lv}^{lv2} = \frac{1}{2} v_{lv2}^{*l+4} \Delta v^* \begin{cases} 1, lv2 = 1 \text{ or } lvm \\ 2, 1 < lv2 < lvm \\ 0, lv2 > lvm \end{cases} + \frac{1}{2} v_{lv2}^{*l+4} v_1^* \delta_1^{lv2} \\ + \begin{cases} \frac{v_{lv2}^{*l+4} (v_{lv} - v_{lvm}^*)}{2} \left[\frac{(v_{lvm+1}^* - v_{lv}) \delta_{lvm}^{lv2} + (v_{lv} - v_{lvm}^*) \delta_{lvm+1}^{lv2}}{\Delta v^*} + \delta_{lvm}^{lv2} \right], & v_{lv} < v_{Nv}^* \\ 0, & v_{lv} \geq v_{Nv}^* \end{cases}. \quad (117)$$

Note that f_β is not expanded for $l \geq 1$, so it is necessary to consider the case where lvm does not exist. In this situation,

$$I_{1lv}^{lv2} = \frac{1}{2} \frac{v_{lv}^2}{v_1^*} \delta_1^{lv2} v_1^{*l+2}, \quad (118)$$

$$I_{2lv}^{lv2} = \frac{1}{2} \frac{v_{lv}^2}{v_1^*} \delta_1^{lv2} v_1^{*l+4}. \quad (119)$$

Besides, we define

$$J_{1lv}^{lv2} = \frac{1}{2} v_{lv2}^{*-l+1} \Delta v^* \begin{cases} 1, lv2 = lvp \\ 2, lv2 > lvp \\ 0, lv2 < lvp \end{cases} + \frac{1}{2} v_{lv2}^{*-l+1} (v_{lv}^* - v_{lv}) \\ \times \left[\begin{cases} \frac{1}{\Delta v^*} \left[(v_{lv}^* - v_{lv}) \delta_{lv}^{lv2} + (v_{lv} - v_{lv}^*) \delta_{lv}^{lv2} \right], & v_{lv} > v_1^* \\ \frac{v_{lv}}{v_1^*} \delta_1^{lv2}, & v_{lv} \leq v_1^* \end{cases} + \delta_{lv}^{lv2} \right], \quad (120)$$

$$J_{2lv}^{lv2} = \frac{1}{2} v_{lv2}^{*-l+3} \Delta v^* \begin{cases} 1, lv2 = lvp \\ 2, lv2 > lvp \\ 0, lv2 < lvp \end{cases} + \frac{1}{2} v_{lv2}^{*-l+3} (v_{lv}^* - v_{lv}) \\ \times \left[\begin{cases} \frac{1}{\Delta v^*} \left[(v_{lv}^* - v_{lv}) \delta_{lv}^{lv2} + (v_{lv} - v_{lv}^*) \delta_{lv}^{lv2} \right], & v_{lv} > v_1^* \\ \frac{v_{lv}}{v_1^*} \delta_1^{lv2}, & v_{lv} \leq v_1^* \end{cases} + \delta_{lv}^{lv2} \right]. \quad (121)$$

Then we define

$$\delta_{lv}^{*lv1} = \begin{cases} \frac{1}{\Delta v^*} \left[(v_{lvm}^* - v_{lv}) \delta_{lvm}^{lv2} + (v_{lv} - v_{lvm}^*) \delta_{lvm+1}^{lv2} \right], & v_{lv} < v_{Nv}^* \\ \frac{v_{lv}}{v_1^*} \delta_1^{lv2}, & lvm \text{ does not exist} \\ 0, & v_{lv} \geq v_{Nv}^* \end{cases} \quad (122)$$

Finally, the elements of $\mathcal{C}_{\text{Ani},00}^{lv1,lv2}_{lv,l(l \geq 1)m}$ are given by

$$\mathcal{C}_{\text{Ani},00}^{lv1,lv2}_{lv,l(l \geq 1)m} = \frac{4\pi}{\mu} \delta_{lv}^{lv1} \delta_{lv}^{lv2} - 4\pi \frac{\mu - 1}{\mu} \partial \delta_{lv}^{lv1} \left(\frac{l+1}{2l+1} v_{lv}^{-l-2} I_{1lv}^{lv2} - \frac{l}{2l+1} v_{lv}^{l-1} J_{1lv}^{lv2} \right) \\ + 2\pi \partial^2 \delta_{lv}^{lv1} \left(C_1 v_{lv}^{-l-3} I_{2lv}^{lv2} + C_1 v_{lv}^l J_{1lv}^{lv2} + C_2 v_{lv}^{-l-1} I_{1lv}^{lv2} + C_2 v_{lv}^{l-2} J_{2lv}^{lv2} \right) \\ + 4\pi \partial \delta_{lv}^{lv1} \left(C_3 v_{lv}^{-l-4} I_{2lv}^{lv2} + C_4 v_{lv}^{l-1} J_{1lv}^{lv2} + C_5 v_{lv}^{-l-2} I_{1lv}^{lv2} + C_6 v_{lv}^{l-3} J_{2lv}^{lv2} \right), \quad (123)$$

where the symbols $\partial\delta$ and $\partial^2\delta$ are the same as those defined in Eqs. (107)–(110). The parameters from C_1 to C_6 are defined as

$$\begin{aligned} C_1 &= \frac{(l+1)(l+2)}{(2l+1)(2l+3)}, \\ C_2 &= \frac{l(l-1)}{(2l+1)(2l-1)}, \\ C_3 &= \frac{-l(l+1)/2 - (l+1)}{(2l+1)(2l+3)}, \\ C_4 &= \frac{-l(l+1)/2 + (l+2)}{(2l+1)(2l+3)}, \\ C_5 &= \frac{l(l+1)/2 + (l-1)}{(2l+1)(2l-1)}, \\ C_6 &= \frac{l(l+1)/2 - l}{(2l+1)(2l-1)}. \end{aligned} \quad (124)$$

To provide the elements of the multidimensional array, we define

$$\partial\delta_{lv}^{lv1} = \begin{cases} \frac{3\delta_1^{lv1} + \delta_2^{lv1}}{3\Delta v}, & l=1 \text{ and } lv=1 \\ \frac{\delta_{lv+1}^{lv1} - \delta_{lv-1}^{lv1}}{2\Delta v}, & l>1 \text{ and } lv \geq l \end{cases}, \quad (125)$$

$$\partial^2\delta_{lv}^{lv1} = \begin{cases} \frac{4\delta_2^{lv1} - 12\delta_1^{lv1}}{3\Delta v^2}, & l=1 \text{ and } lv=1 \\ \frac{\delta_{lv+1}^{lv1} - 2\delta_{lv}^{lv1} + \delta_{lv-1}^{lv1}}{\Delta v^2}, & l>1 \text{ and } lv \geq l \end{cases}. \quad (126)$$

Then the elements of $\mathcal{C}_{\text{Ani},lm}^{lv1,lv2}_{lv,l(l \geq 1)m}$ are given by

$$\begin{aligned} \mathcal{C}_{\text{Ani},lm}^{lv1,lv2}_{lv,l(l \geq 1)m} &= \frac{4\pi}{\mu} \delta_{lv}^{lv1} \delta_{lv}^{*lv2} - 4\pi \frac{\mu-1}{\mu} v^{-2} I_{2lv}^{lv2} \partial\delta_{lv}^{lv1} + \frac{4\pi}{3} \left(v^{-3} I_{3lv}^{lv2} + I_{1lv}^{lv2} \right) \partial^2\delta_{lv}^{lv1} \\ &\quad + \frac{4\pi}{3} \left(-v^{-4} I_{3lv}^{lv2} + 2v^{-1} I_{1lv}^{lv2} + 3v^{-2} I_{2lv}^{lv2} \right) \partial\delta_{lv}^{lv1} \\ &\quad - \frac{2\pi}{3} l(l+1) \left(-v^{-5} I_{3lv}^{lv2} + 2v^{-2} I_{1lv}^{lv2} + 3v^{-3} I_{2lv}^{lv2} \right) \delta_{lv}^{lv1}, \end{aligned} \quad (127)$$

where the definition of δ^* is the same as Eq. (106), and the definitions of I_1 , I_2 , and I_3 are the same as Eqs. (99)–(101), (104) and (105).

The arrays of electric current are given by

$$\begin{aligned} \mathcal{J}_{x,\alpha}^{lv0} &= \frac{4\pi}{3} Z_\alpha r_{lv0} v_{lv0}^3 \Delta v, \\ \mathcal{J}_{y,\alpha}^{lv0} &= \frac{8\pi}{3} Z_\alpha r_{lv0} v_{lv0}^3 \Delta v, \\ \mathcal{J}_{z,\alpha}^{lv0} &= -\frac{8\pi}{3} Z_\alpha r_{lv0} v_{lv0}^3 \Delta v. \end{aligned} \quad (128)$$

And arrays related to laser propagation are given by

$$S_r^{lx0} = \begin{cases} \frac{1}{2\Delta x} (\delta_{lx+1}^{lv0} - \delta_{lx-1}^{lx0}), & lx < N_x \\ \frac{1}{2\Delta x} (3\delta_{lx}^{lv0} - 4\delta_{lx-1}^{lv0} + \delta_{lx-2}^{lv0}), & lx = N_x \end{cases}, \quad (129)$$

$$S_l^{lx0} = \begin{cases} \frac{1}{2\Delta x} (\delta_{lx+1}^{lv0} - \delta_{lx-1}^{lx0}), & lx > 1 \\ \frac{1}{2\Delta x} (-3\delta_{lx}^{lv0} + 4\delta_{lx+1}^{lv0} - \delta_{lx+2}^{lv0}), & lx = 1 \end{cases}, \quad (130)$$

$$\mathcal{L}_l(t)_{lx} = \frac{\delta_{lx}^1}{2\Delta x} F_{tl}(t), \quad (131)$$

$$\mathcal{L}_r(t)_{lx} = \frac{\delta_{lx}^{N_x}}{2\Delta x} F_{tr}(t), \quad (132)$$

where $F_{tl}(t)$ and $F_{tr}(t)$ represent the transverse fields of the left and right incident lasers.

References

- [1] R.C. Malone, R.L. McCrory, R.L. Morse, *Phys. Rev. Lett.* 34 (1975) 721.
- [2] A.R. Bell, R.G. Evans, D.J. Nicholas, *Phys. Rev. Lett.* 46 (1981) 243.
- [3] A.V. Brantov, V.Yu. Bychenkov, V.T. Tikhonchuk, W. Rozmus, *J. Exp. Theor. Phys.* 83 (1996) 716.
- [4] B. Appelbe, M. Sherlock, O. El-Amiri, C. Walsh, J. Chittenden, *Phys. Plasmas* 26 (2019) 102704.
- [5] Hanzhi Zhao, Zhengming Sheng, Suming Weng, *Matter Radiat. Extrem.* 7 (2022) 045901.
- [6] P.W. Rambo, S.C. Wilks, W.L. Kruer, *Phys. Rev. Lett.* 79 (1997) 83.
- [7] C.J. Pawley, H.E. Huey, N.C. Luhmann, *Phys. Rev. Lett.* 49 (1982) 877.
- [8] U. Czarnetzki, L.L. Alves, *Rev. Mod. Plasma Phys.* 6 (2022) 31.
- [9] George H. Miller, Edward I. Moses, Craig R. Wuest, *Nucl. Fusion* 44 (2004) S228.
- [10] J. Ebrardt, J.M. Chaput, *J. Phys. Conf. Ser.* 244 (2010) 032017.
- [11] John Lindl, *Phys. Plasmas* 2 (1995) 3933.
- [12] John D. Lindl, Peter Amendt, Richard L. Berger, S. Gail Glendinning, Siegfried H. Glenzer, Steven W. Haan, Robert L. Kauffman, Otto L. Landen, Laurence J. Suter, *Phys. Plasmas* 11 (2004) 339.
- [13] David S. Montgomery, *Phys. Plasmas* 23 (2016) 055601.
- [14] John D. Lindl, Peter Amendt, Richard L. Berger, S. Gail Glendinning, Siegfried H. Glenzer, Steven W. Haan, Robert L. Kauffman, Otto L. Landen, Laurence J. Suter, *Phys. Plasmas* 11 (2004) 339.
- [15] D.E. Hinkel, M.D. Rosen, E.A. Williams, A.B. Langdon, C.H. Still, D.A. Callahan, J.D. Moody, P.A. Michel, R.P.J. Town, R.A. London, S.H. Langer, *Phys. Plasmas* 18 (2011) 056312.
- [16] R.L. Berger, C.A. Thomas, K.L. Baker, D.T. Casey, C.S. Goyon, J. Park, N. Lemos, S.F. Khan, M. Hohenberger, J.L. Milovich, D.J. Strozzi, M.A. Belyaev, T. Chapman, A.B. Langdon, *Phys. Plasmas* 26 (2019) 012709.
- [17] D.W. Forslund, J.M. Kindel, W.B. Mori, C. Joshi, J.M. Dawson, *Phys. Rev. Lett.* 54 (1985) 558.
- [18] Q. Wang, C.Y. Zheng, Z.J. Liu, C.Z. Xiao, Q.S. Feng, H.C. Zhang, X.T. He, *Plasma Phys. Control. Fusion* 60 (2017) 025016.
- [19] Yu Ji, Chang-Wang Lian, Rui Yan, Chuang Ren, Dong Yang, Zhen-Hua Wan, Bin Zhao, Chen Wang, Zhi-Heng Fang, Jian Zheng, *Matter Radiat. Extrem.* 6 (2021) 015901.
- [20] Tao Gong, Liang Hao, Zhichao Li, Dong Yang, Sanwei Li, Xin Li, Liang Guo, Shiyang Zou, Yaoyuan Liu, Xiaohua Jiang, Xiaoshi Peng, Tao Xu, Xiangming Liu, Yulong Li, Chunyang Zheng, Hongbo Cai, Zhanjun Liu, Jian Zheng, Zhebin Wang, Qi Li, Ping Li, Rui Zhang, Ying Zhang, Fang Wang Deen Wang, Feng Wang, Shenye Liu, Jiamin Yang, Shaoen Jiang, Baohan Zhang, Yongkun Ding, *Matter Radiat. Extrem.* 4 (2019) 055202.
- [21] A. Pak, E.L. Dewald, O.L. Landen, J. Milovich, D.J. Strozzi, L.F. Berzak Hopkins, D.K. Bradley, L. Divol, D.D. Ho, A.J. MacKinnon, N.B. Meezan, P. Michel, J.D. Moody, A.S. Moore, M.B. Schneider, R.P.J. Town, W.W. Hsing, M.J. Edwards, *Phys. Plasmas* 22 (2015) 122701.
- [22] E.M. Epperlein, R.W. Short, A. Simon, *Phys. Rev. Lett.* 69 (1992) 1765.
- [23] M.D. Tracy, E.A. Williams, K.G. Estabrook, J.S. De Groot, S.M. Cameron, *Phys. Fluids B* 5 (1993) 1430.
- [24] S.T. Zhang, Y.Z. Zhou, T. Yang, R. Xie, Y. Jiang, S.S. Ban, Q.S. Feng, Y.X. Wang, B. Qiao, Z.J. Liu, L.H. Cao, C.Y. Zheng, *Plasma Phys. Control. Fusion* 63 (2021) 045014.
- [25] A.J. Kemp, F. Fiuza, A. Debayle, T. Johzaki, W.B. Mori, P.K. Patel, Y. Sentoku, L.O. Silva, *Nucl. Fusion* 54 (2014) 054002.
- [26] A.P.L. Robinson, D.J. Strozzi, J.R. Davies, L. Gremillet, J.J. Honrubia, T. Johzaki, R.J. Kingham, M. Sherlock, A.A. Solodov, *Nucl. Fusion* 54 (2014) 054003.
- [27] H. Shiraga, H. Nagatomo, W. Theobald, A.A. Solodov, M. Tabak, *Nucl. Fusion* 54 (2014) 054005.
- [28] J. Badziak, S. Jabłoński, J. Wołoski, *Plasma Phys. Control. Fusion* 49 (2007) B651.
- [29] P.A. Norreys, R. Allott, R.J. Clarke, J. Collier, D. Neely, S.J. Rose, *Phys. Plasmas* 7 (2000) 3721.
- [30] E. Michael Campbell, Richard R. Freeman, Kazuo A. Tanaka, *Fusion Sci. Technol.* 49 (2006) 249.
- [31] M. Tabak, P. Norreys, V.T. Tikhonchuk, K.A. Tanaka, *Nucl. Fusion* 54 (2014) 054001.
- [32] Stefano Atzeni, *Phys. Plasmas* 6 (1999) 3316.
- [33] M.H. Key, *Phys. Plasmas* 14 (2007) 055502.
- [34] R. Kodama, H. Shiraga, K. Shigemori, Y. Toyama, S. Fujioka, H. Azechi, H. Fujita, H. Habara, T. Hall, Y. Izawa, T. Jitsuno, Y. Kitagawa, K.M. Krushelnick, K.L. Lancaster, K. Mima, K. Nagai, M. Nakai, H. Nishimura, T. Norimatsu, P.A. Norreys, S. Sakabe, K.A. Tanaka, A. Youssef, M. Zepf, T. Yamanaka, *Nature* 418 (2002) 933.
- [35] R.L. Berger, E.J. Valeo, *Phys. Plasmas* 12 (2005) 032104.
- [36] Z.J. Liu, C.Y. Zheng, X.T. He, Yugang Wang, *Phys. Plasmas* 18 (2011) 032705.
- [37] J.M. Dawson, *Rev. Mod. Phys.* 55 (1983) 403.
- [38] H. Okuda, *J. Comput. Phys.* 10 (1972) 475.
- [39] J.S. Chang, G. Cooper, *J. Comput. Phys.* 6 (1970) 1.
- [40] C.Z. Cheng, Georg Knorr, *J. Comput. Phys.* 22 (1976) 330.
- [41] J.P. Matte, J. Virmont, *Phys. Rev. Lett.* 49 (1982) 1936.
- [42] E.M. Epperlein, G.J. Rickard, A.R. Bell, *Phys. Rev. Lett.* 61 (1988) 2453.
- [43] A.B. Langdon, *Phys. Rev. Lett.* 44 (1980) 575.
- [44] F. Alouani-Bibi, M.M. Shoucri, J.P. Matte, *Comput. Phys. Commun.* 164 (2004) 60.
- [45] S. Mijin, A. Antony, F. Militello, R.J. Kingham, *Comput. Phys. Commun.* 258 (2021) 107600.
- [46] Ruo Li, Yinu Ren, Yanli Wang, *J. Comput. Phys.* 434 (2021) 110235.
- [47] O. Larroche, *Eur. Phys. J. D* 27 (2003) 131.
- [48] W.T. Taitano, L. Chacón, A.N. Simakov, *Comput. Phys. Commun.* 365 (2018) 173.
- [49] W.T. Taitano, B.D. Keenan, L. Chacón, S.E. Anderson, H.R. Hamer, A.N. Simakov, *Comput. Phys. Commun.* 263 (2021) 107861.
- [50] R.J. Kingham, A.R. Bell, *J. Comput. Phys.* 194 (2004) 1.
- [51] A.G.R. Thomas, R.J. Kingham, C.P. Ridgers, *New J. Phys.* 11 (2009) 033001.
- [52] Jan Nikl, Ilja Göthel, Milan Kuchařík, Stefan Weber, Michael Bussmann, *J. Comput. Phys.* 434 (2021) 110214.
- [53] M. Sherlock, *Phys. Plasmas* 16 (2009) 103101.
- [54] Roland Duclos, Bruno Dubroca, Francis Filbet, Vladimir Tikhonchuk, *J. Comput. Phys.* 228 (2009) 5072.
- [55] M.J. Keskinen, *Phys. Rev. Lett.* 103 (2009) 055001.
- [56] A.R. Bell, A.P.L. Robinson, M. Sherlock, R.J. Kingham, W. Rozmus, *Plasma Phys. Control. Fusion* 48 (2006) R37.
- [57] M. Sherlock, A.R. Bell, W. Rozmus, *Laser Part. Beams* 24 (2006) 231.
- [58] M. Tzoufras, A.R. Bell, P.A. Norreys, F.S. Tsung, *J. Comput. Phys.* 230 (2011) 6475.
- [59] H.C. Yee, *J. Comput. Phys.* 68 (1987) 151–179.
- [60] M.N. Rosenbluth, W.M. MacDonald, D.L. Judd, *Phys. Rev.* 107 (1957) 1.
- [61] I.P. Shkarofsky, M.M. Shoucri, V. Fuchs, *Comput. Phys. Commun.* 71 (1992) 269.
- [62] W.L. Kruer, *The Physics of Laser Plasma Interactions*, Addison-Wesley, Redwood City, CA, 1988.
- [63] F.F. Chen, *Introduction to Plasma Physics and Controlled Fusion*, Springer International Publishing, Cham, 2016, pp. 124–125.
- [64] Z.J. Liu, B. Li, J. Xiang, L.H. Cao, C.Y. Zheng, L. Hao, *Plasma Phys. Control. Fusion* 60 (2018) 045008.
- [65] S.I. Braginskii, in: M.A. Leontovich (Ed.), *Reviews of Plasma Physics*, vol. 1, Consultants Bureau, New York, 1965, p. 205.
- [66] O. Klimo, V.T. Tikhonchuk, X. Ribeyre, G. Schurtz, C. Riconda, S. Weber, J. Limpouch, *Phys. Plasmas* 18 (2011) 082709.
- [67] W. Rozmus, A.V. Brantov, M. Sherlock, V.Yu. Bychenkov, *Plasma Phys. Control. Fusion* 60 (2018) 014004.
- [68] C.F.F. Karney, *Comput. Phys. Rep.* 4 (1986) 183–244.
- [69] J.W. Banks, S. Brunner, R.L. Berger, T.M. Tran, *Phys. Plasmas* 23 (2016) 032108.